

Making the Subdominant Dominant: Gravothermal Pile-Up of Collisional Dark Matter Around Compact Objects

Reza Ebadi^{1,*} and Erwin H. Tanin^{2,†}

¹*Department of Physics, University of Maryland, College Park, Maryland 20742, USA*

²*Stanford Institute for Theoretical Physics, Stanford University, Stanford, California 94305, USA*

The dark matter may consist of multiple species that interact differently. We show that a species that is cosmologically subdominant but highly collisional can pile up and become dominant in deep gravitational wells, such as those of white dwarfs and neutron stars.

Proposed extensions to the Standard Model (SM) often include new particles, either as necessary ingredients or unintended byproducts. Some of these particles are expected to account for the observed dark matter (DM) abundance in the universe. Their self-interaction cross-section-to-mass ratios are constrained to be $\sigma_m \lesssim 1 \text{ cm}^2/\text{g}$ [1–3], with a possible preference toward the upper end if the self-interacting DM (SIDM) picture [4–6] holds [7, 8]. The rest generically constitute tiny ($\lesssim 10\%$) subcomponents of the total DM and have virtually unconstrained self-interactions. In this paper, we demonstrate that subcomponents that are cosmologically insignificant can rise to importance locally, e.g., around compact objects, if they self-interact sufficiently strongly.

We consider a subcomponent with arguably the simplest type of self-interaction, namely elastic and velocity-independent collision, but with an extremely large σ_m . Motivated by σ_m values found in the SM, we focus on σ_m in the range $10 - 10^{10} \text{ cm}^2/\text{g}$, although larger values are not ruled out observationally. The lower and upper ends of this range are close to the σ_m of a nucleus and a molecule. We will show that subcomponents with such a large σ_m pile up in deep gravitational wells, so much so that they can far dominate the DM mass density locally. Thermal pressure poses a hurdle to the pile-up, but heat conduction enabled by elastic collisions relieves the pressure support gradually, allowing the piling to continue. This mechanism, we dub *gravothermal pile up*, may occur in many setups. Here, we focus on white dwarfs (WDs) and neutron stars (NSs) in galactic environment.

Scenarios where subcomponents of DM self-interact appreciably have previously been explored. Models with large elastic σ_m , akin to the type we consider, have been proposed to explain the origin of supermassive black holes [9–11], but they are yet to be explored at much smaller length scales. Other works focused mainly on subcomponents with dissipative self-interactions, a possibility largely motivated by the mirror-world scenario [12–20] and often called partially interacting dark matter [21, 22]. Consequences of a dissipative dark sector include the formation of a dark disk [21], novel indirect detection signatures [21, 23], dark acoustic oscillations [24, 25], formation of compact structures [26–28], among others [29–34].

Boltzmann’s Equilibrium.— Given an ambient gas of collisional particles χ with mass density ρ_χ^∞ and

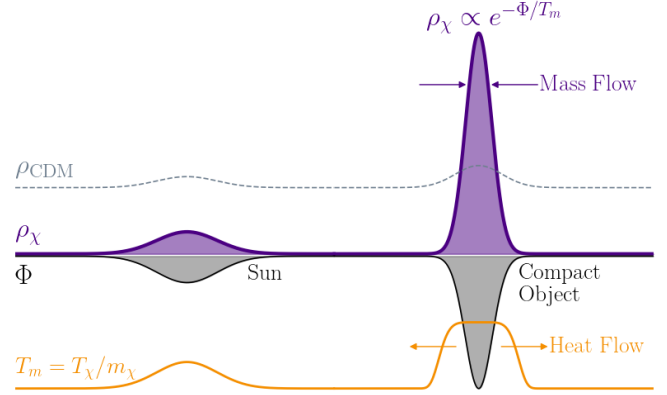


FIG. 1. Gravothermal pile-up mechanism. Collisionless cold dark matter (CDM) transiting through a gravitational well gets mildly focused. Collisional DM subcomponent χ instead piles up gravothermally: as heat flows out through conduction, decreased pressure lets more χ particles to flow in. Around a sufficiently deep gravitational well Φ , the subcomponent χ can be locally dominant over the CDM.

temperature per unit mass T_m^∞ , we introduce a fixed central gravitational well $\Phi(r) < 0$ that vanishes at infinity. It is well known that the gas will seek the Boltzmann-enhanced density profile $\rho_\chi^{\text{eq}}(r) = \rho_\chi^\infty e^{-\Phi(r)/T_m^\infty}$, which could be substantially enhanced if $-\Phi \gg T_m^\infty$, reflecting a propensity of the gas to collect in the well. This density profile is that of an ideal gas in hydrostatic equilibrium, if it could establish a global thermal equilibrium, $T_m(r) = T_m^\infty$. In reality, global thermalization takes time, and the gas may only thermalize locally, with some temperature profile $T_m(r) > T_m^\infty$. For each $T_m(r)$, there is a unique density profile that yields hydrostatic equilibrium,

$$\rho_\chi(r) = \rho_\chi^\infty \frac{T_m^\infty}{T_m(r)} e^{-\int_\infty^r dr' \frac{\partial_{r'} \Phi(r')}{T_m(r')}} \quad (1)$$

If there exists a region $r \leq r_{\text{iso}}$ where the temperature is approximately uniform, $T_m(r) \approx T_m^{\text{iso}} > T_m^\infty$, the density profile inside this isothermal region is $\rho_\chi^{\text{iso}}(r) \propto e^{-\Phi(r)/T_m^{\text{iso}}}$, which is similar to ρ_χ^{eq} apart from a prefactor that depends on profiles exterior to the isothermal region. Therefore, in this case an exponentially enhanced

TABLE I. Benchmark properties of compact objects.

	$M_\star [M_\odot]$	$R_\star [\text{km}]$	v_{esc}	$t_{\text{age}} [\text{Gyr}]$
white dwarf	1	6000	0.02	10
neutron star	1.4	10	0.6	10

overdensity could still occur if $-\Phi/T_m^{\text{iso}} \gtrsim \text{few}$.

To what degree the global thermal equilibrium is approached is a dynamical, history-dependent question. When the gas first settles into a hydrostatic equilibrium, its temperature typically rises to $T_m \sim -\Phi$, through a combination of shock and compressional heating. Subsequently, the system evolves toward global thermalization gravothermally: collisions cause heat to flow outward through conduction, cooling the central gas gradually and allowing mass to flow inward to re-establish hydrostatic equilibrium with higher density, as per Eq. (1). This gravothermal pile-up process is illustrated in Fig. 1. The final temperature profile and, correspondingly, the amount of density enhancement will be determined by the efficiency of the heat conduction.

Significant gravothermal pile-up may occur around a potential whose escape velocity is v_{esc} if the environment has $T_m^\infty \ll v_{\text{esc}}^2/2$. As a start, we will adopt a galactic environment, where typically $T_m^\infty \sim 10^{-6}$. For instance, in Milky Way the Sun's core already satisfies the requisite condition with its $v_{\text{esc}}^2/2 \approx G(0.5M_\odot)/(0.2R_\odot) = 5 \times 10^{-6}$, albeit marginally. Any solar-mass objects more compact than the Sun are even better sites for gravothermal pile-up. We will focus on WDs and NSs with benchmark properties shown in Table I.

Setup.— We assume that particles χ with cross-section-to-mass ratio $\sigma_m \gg 1 \text{ cm}^2/\text{g}$ are present in galaxies with typical density and temperature per unit mass

$$\rho_\chi^\infty = f \times 0.4 \text{ GeV}/\text{cm}^3, \quad T_m^\infty = 10^{-6} \quad (2)$$

where $f \lesssim 10\%$. During structure formation, the dominant DM provides potential wells that the χ gas falls into. A priori, due to its collisional nature, the χ distribution need not necessarily follow that of the dominant DM at the scales of nonlinear structures. This leads to the question of how the subcomponent fraction in a typical DM halo f relates to the cosmic fraction $\bar{f} = \Omega_\chi/\Omega_{\text{DM}}$. We expect the subcomponent to behave as non-radiative perfect fluid on DM-halo scales,¹ much like the SM baryon

gas, but with the radiative cooling turned off. Incidentally, simulations of structure formation in vanilla cosmology with a non-radiative fluid subcomponent added to the mix have been performed extensively in the past. They were used to test assumptions on the main mechanisms determining the baryon fraction of DM halos, including the roles of gas cooling. In short, these simulations suggest that $f \simeq 0.9\bar{f}$ across a wide range of DM halo masses; from $10^{15} M_\odot$ (clusters) to $10^{10} M_\odot$ (dwarfs) [35], and extending down to $10^7 M_\odot$ (ultra-faint dwarfs) and even $10^4 M_\odot$ (minihalos) [36]. These studies also indicate that the subcomponent's density distributions within halos follow the standard NFW profile.² Furthermore, analytical arguments based on self-similar solutions to fluid equations led to similar conclusions [39].

We are interested in the accumulation of a galactic population of χ particles around a compact object of mass M_\star and radius R_\star . To model this process, we employ the *gravothermal* formalism, which was developed to model stellar dynamics in a globular cluster [40] and, more recently, applied to SIDM scenarios [41, 42]. It is based on three equations: (1) $\vec{\nabla}(\rho_\chi T_m) = -\rho_\chi \vec{\nabla}\Phi$, (2) $\rho_\chi T_m \dot{s} = -\vec{\nabla} \cdot \vec{\mathcal{F}}$, (3) $\vec{\mathcal{F}} = -\kappa_{\text{eff}} \vec{\nabla} T_m$, which describe, respectively, quasi-hydrostatic equilibrium, the first law of thermodynamics, and Fourier's law of conduction. Here, $s \equiv \ln(T_m^{3/2}/\rho_\chi)$ is the specific entropy of the gas up to additive constants, $\vec{\mathcal{F}}$ is the conductive heat flux, $\kappa_{\text{eff}} \sim \rho_\chi^2 \sigma_m \sqrt{T_m} (r^{-2} + \lambda_{\text{mfp}}^{-2})^{-1}$ is the effective conductivity, and $\lambda_{\text{mfp}} \equiv (\rho_\chi \sigma_m)^{-1}$ is the mean free path. We further assume that the system is spherically symmetric and neglect χ 's contribution to the gravitational potential Φ . For more details, see the Supplemental Material.

Important timescales of our setup include: the collisional timescale $\tau_{\text{col}} \equiv \lambda_{\text{mfp}}/\sqrt{T_m}$, the sound-crossing timescale $\tau_{\text{sound}} \equiv r/\sqrt{T_m}$, and the heat-conduction timescale $\tau_{\text{cond}} \equiv |\dot{s}|^{-1} \sim \tau_{\text{col}}(1 + r^2/\lambda_{\text{mfp}}^2)$. The gravothermal approach implicitly assumes that hydrostatic and local thermal equilibrium are rapidly established. These are justified if both τ_{col} and τ_{sound} are shorter than τ_{cond} . We checked that these requirements are always satisfied.³ The longest timescale we will consider is $t_{\text{age}} = 10 \text{ Gyr}$, thus, as a minimum requirement,

free path matches the system size, the subcomponent in that regime may behave very differently from perfect fluid. Nevertheless, this will not affect our results as we will express them in terms of the galactic fraction f rather than the cosmic fraction \bar{f} .

²The results of these simulations depend on the initial cosmic temperature of the subcomponent prior to structure formation; higher temperatures tend to suppress its fraction in the central region of the CDM halo. For initial temperatures comparable to or less than that of realistic baryonic gas ($\sim 10 \text{ meV}$) the suppression is not significant. Also, these simulations are not to be confused with those that studied the fluid limit of SIDM as the *dominant* DM, which found that the resulting halos resemble cuspy isothermal spheres, with density profiles $\rho_\chi(r) \propto r^{-2}$ [37, 38].

³When $\lambda_{\text{mfp}} \gtrsim r$, the local-thermalization condition, $\tau_{\text{col}} \lesssim \tau_{\text{cond}}$,

¹The mean free path of the subcomponent is negligible at the scale of 10 kpc if $f\sigma_m \gtrsim 100 \text{ cm}^2/\text{g}$. This is satisfied in nearly all the parameter space we consider, except for the $f\sigma_m \sim 1 - 100 \text{ cm}^2/\text{g}$ range. Since the efficiency of heat conduction peaks when the mean

White Dwarf

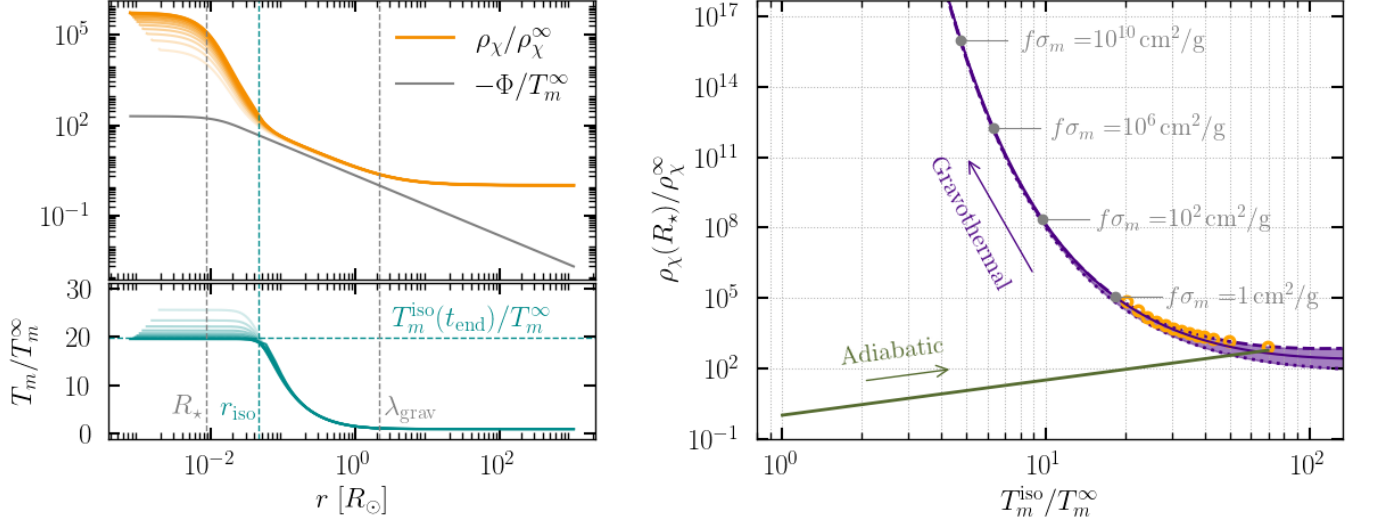


FIG. 2. Results of a gravothermal simulation of subcomponent particles χ accumulating around the benchmark WD of Table I. *Left*: Snapshots of χ 's density ρ_χ , χ 's temperature per unit mass T_m , and the WD's gravitational potential Φ , rescaled by the ambient values, ρ_χ^∞ and T_m^∞ , as indicated. The radius R_\star and gravitational-influence radius λ_{grav} of the WD as well as the radius $r_{\text{iso}}(t_{\text{end}})$ and temperature $T_m^{\text{iso}}(t_{\text{end}})/T_m^\infty$ of the isothermal core at the end of the simulation are marked. *Right*: Central density $\rho_\chi(R_\star)$ vs isothermal-core temperature T_m^{iso} phase space, rescaled as indicated. The system first evolves adiabatically to reach the hydrostatic state of Eq. (3), before proceeding to cool and pile up gravothermally. The orange circles are representative points from the simulation. The purple curves are theoretical expectations based on three different assumptions on the T_m profile outside of the isothermal core: (1) the initial adiabatic profile (dashed), (2) the steady-state profile with $\dot{s} \propto -\vec{\nabla} \cdot \vec{\mathcal{F}} \approx 0$ (dotted), and (3) $\eta_{\text{eff}} = 1$, a simplifying assumption used in the main text (solid). Subcomponents with different f and σ_m values evolve along the same evolution curve at rates proportional to $f\sigma_m$ and reach different terminal points after 10 Gyr (the age of the WD), as indicated in gray dots. Apart from that, other features of both plots apply equally for all f and σ_m values.

we assume that the ambient χ gas has $\tau_{\text{col}} \ll t_{\text{age}}$, which amounts to $f\sigma_m \gg 1$ cm²/g. Furthermore, we assume that within a timescale $\tau_{\text{sound}} \ll \tau_{\text{cond}}$, the subcomponent gas rearranges itself isentropically to establish a hydrostatic equilibrium around the compact object. The resulting configuration can be found from Eq. (1), after equating the specific entropy to that of the mean background $s_\chi^\infty = \ln[(T_m^\infty)^{3/2}/\rho_\chi^\infty]$, to be

$$T_m^{\text{ad}}(r) = T_m^\infty - \frac{2}{5}\Phi(r), \quad \rho_\chi^{\text{ad}}(r) = \rho_\chi^\infty \left(\frac{T_m^{\text{ad}}(r)}{T_m^\infty} \right)^{3/2} \quad (3)$$

which we refer to as the adiabatic temperature and density profiles. These serve as an initial condition for the subsequent gravothermal evolution.⁴

Gravothermal Pile-Up.— Here, we discuss the subsequent buildup dynamics of χ particles around gravitational wells. We base our analysis on the results of gravothermal simulations we ran using the code developed by [9] and re-implemented by [47–49]. We modified the codebase provided in [50] to adapt it to our setup, with a major update of switching from a self-gravitating system to that with fixed external gravitational potential. This code discretizes the subcomponent gas into concentric spherical shells, and evolves the shells by alternating between (1) a heat conduction step for each shell that brings the system out of hydrostatic equilibrium and (2) isentropic repositioning of shells to reestablish hydrostatic equilibrium. More details about the code are provided in the Supplemental Material.

holds only marginally. Nevertheless, the results of gravothermal (with proper calibration of the conductivity coefficients) and N-body simulations have been shown to agree well even in those marginal cases [43–46].

⁴Although the temperature profile of Eq. (3) is consistent with the boundary condition $T_m(r \rightarrow \infty) = T_m^\infty$, it behaves as $T_m^{\text{ad}} - T_m^\infty \propto r^{-1}$ beyond the radius of gravitational influence of the compact object $\lambda_{\text{grav}} \equiv GM_\star/T_m^\infty$. Thus, such a profile leads to an unphysical

heat-conduction luminosity that is growing as $L \equiv 4\pi r^2 \mathcal{F} \propto r^2$ at $r \gtrsim \lambda_{\text{grav}}$. The details of the small deviation $T_m - T_m^\infty$ are important because L depends on $\partial_r T_m$ and not just T_m . In reality, collisions of the χ gas bound to the compact object with the ambient, unbound gas (which are important only at $r \gtrsim \lambda_{\text{grav}}$) would bring T_m exponentially close to T_m^∞ after several τ_{col} . To account for this effect, in practice we introduce an exponential factor to the T_m^{ad} profile to make it decay faster: $T_m^{\text{ad}} = T_m^\infty - (2/5)\Phi e^{-r^2/\lambda_{\text{grav}}^2}$.

In the $\lambda_{\text{mfp}} \gg r$ limit, the gravothermal evolution equations are invariant under simultaneous rescalings of $f\sigma_m \rightarrow \alpha \times f\sigma_m$ and $t \rightarrow \alpha^{-1} \times t$. Thus, subcomponents with different $f\sigma_m$ values go through the same series of movie frames (spatial profiles) with rates proportional to $f\sigma_m$. Formally, the solutions for the density and temperature profiles can be written as $\rho_\chi = \rho_\chi^\infty \mathcal{T}_\rho(f\sigma_m t, r)$ and $T_m = T_m^\infty \mathcal{T}_T(f\sigma_m t, r)$, where \mathcal{T}_ρ and \mathcal{T}_T are transfer functions with the indicated dependencies. Note that ρ_χ carries an additional f -dependence through the boundary condition $\rho_\chi^\infty \propto f$ that is not captured by \mathcal{T}_ρ . Regardless, the evolution of $\rho_\chi/\rho_\chi^\infty$ and T_m/T_m^∞ depends on f and σ_m only through the combination $f\sigma_m t$.

We performed gravothermal simulations for the accumulation of subcomponent around WD up to $t_{\text{end}} = 0.8 \text{ Gyr}[f\sigma_m/(\text{cm}^2/\text{g})]^{-1}$. We plot in Fig. 2 snapshots of the simulated temperature and density profiles. From these results, we could infer that, almost immediately, heat conduction thermalizes the χ gas near the center, forming an isothermal core. The adiabatic profile outside the core remains essentially frozen at first. Subsequently, the isothermal core cools down by transferring heat to its vicinity, growing in size and mass as a result. The profile exterior to the core develops inside out: heat conduction thaws the profile as its effect spreads to larger radii, and the thawed parts seem to evolve toward a stationary shape characterized by the lack of heat sink/source, $\dot{s} \propto -\vec{\nabla} \cdot \vec{\mathcal{F}} = 0$, whereupon the profile, again, freezes. We note that a similar tendency is found in other systems [42, 51–53]. We did not simulate NS since it is significantly more expensive computationally, but expect the results to be qualitatively the same as that for WD.

The simulation eventually becomes prohibitively expensive as the timestep required to keep it reliable becomes extremely small. While we have simulation results up to $t = 0.8 \text{ Gyr}$ for $f\sigma_m \sim 1 \text{ cm}^2/\text{g}$, in much of the interesting (f, σ_m) parameter space, namely those with $f\sigma_m \gg 1 \text{ cm}^2/\text{g}$, a 10 Gyr run time is beyond our practical reach. In order to determine the final configurations of the χ -particle piles around compact objects, we develop an analytical model of the gravothermal evolution that captures salient aspects of our simulation results. Our simulations suggest that in general the temperature profile can be divided into two regions: the isothermal core and the exterior. We approximate the temperature profile inside the isothermal core as exactly uniform and write the full profile as

$$T_m(r) = T_m^{\text{iso}} \Theta(r_{\text{iso}} - r) + T_m^{\text{ext}}(r) \Theta(r - r_{\text{iso}}) \quad (4)$$

It suffices to specify the temperature profile, $T_m(r)$, as other properties of a χ pile can be derived from it. We denote the corresponding hydrostatic density profiles, given by Eq. (1), as $\rho_\chi^{\text{iso/ext}}$. Given a T_m^{ext} , we define r_{iso} precisely as the radius at which $\partial_r T_m^{\text{ext}} = (T_m^\infty - T_m^{\text{iso}})/r_{\text{iso}}$. Using the above temperature profile, we are able to reduce the three gravothermal partial differential equations

into a single integro-differential equation for the time evolution of T_m^{iso}

$$\dot{T}_m^{\text{iso}} \approx \frac{[r^2 \kappa_{\text{eff}}^{\text{ext}} \partial_r T_m^{\text{ext}}]_{r=r_{\text{iso}}}}{\int_0^{r_{\text{iso}}} r^2 dr \rho_\chi^{\text{iso}} \left(\frac{3}{2} - \frac{\partial \ln \rho_\chi^{\text{iso}}}{\partial \ln T_m^{\text{iso}}} \right)} \quad (5)$$

where $\kappa_{\text{eff}} \approx r^2 \rho_\chi^2 \sigma_m \sqrt{T_m}$ for $\lambda_{\text{mfp}} \gg r$, which is satisfied in all the parameter space we consider at $r = r_{\text{iso}}$. We assume the initial condition $T_m^{\text{iso}}(t=0) = T_m^{\text{ad}}(r=R_\star)$, although the final results are not sensitive to this choice. Eq. (5) can be solved numerically once the exterior temperature profile T_m^{ext} is specified, which we discuss next.

The density profile inside the isothermal core is given by Eq. (1) and can be expressed as

$$\frac{\rho_\chi^{\text{iso}}(r)}{\rho_\chi^\infty} = (2\eta_{\text{iso}})^{2\bar{\eta}} \left(\frac{T_m^{\text{iso}}}{T_m^\infty} \right)^{2\bar{\eta}-1} e^{-\frac{\Phi(r)}{T_m^{\text{iso}}} - 2\eta_{\text{iso}}}, \quad \eta \equiv \frac{r \partial_r \Phi}{2T_m^{\text{ext}}} \quad (6)$$

where $\bar{\eta} \equiv [\int_{r_{\text{iso}}}^\infty \frac{dr}{r} \eta] / [\ln(\lambda_{\text{grav}}/r_{\text{iso}})]$, $\eta_{\text{iso}} \equiv \eta(r_{\text{iso}})$, and $\lambda_{\text{grav}} \equiv GM_\star/T_m^\infty$ is the compact object's radius of gravitational influence. The quantity η encapsulates aspects of the external profiles that are relevant to our analysis. It also measures the conformity of T_m^{ext} with the virial theorem, which predicts $\langle r \partial_r \Phi \rangle / 2T_m^{\text{ext}} = 1$, for a particle in potential Φ in 1D. Indeed, η in general does not deviate much from unity. In our simulations, the η profile starts with that corresponding to the adiabatic profile of Eq. 3 and evolves toward the η of the steady temperature profile $T_m^{\text{st}} \approx T_m^\infty + (4GM_\star/7r)e^{-7r/4\lambda_{\text{grav}}}$ obtained from the stationary condition $\dot{s} \propto -\vec{\nabla} \cdot \vec{\mathcal{F}} \approx 0$ and Eq. 1. Throughout the evolution, the η_{iso} and $\bar{\eta}$ remain close to unity. See the Supplemental Material for more details. In Fig. 2, we display the ρ_χ^{iso} at $r = R_\star$ as a function of T_m^{iso} , for different η assumptions. It is apparent that the different η assumptions amount to mild $\mathcal{O}(1)$ variation in $\rho_\chi(R_\star)$ and does not significantly affect the overall trend, especially at late times.

To simplify our analysis, in what follows we will set η_{iso} and $\bar{\eta}$ to an effective constant η_{eff} ; a more complete account of η is given in the Supplemental Material. We solved the heat equation numerically and found that the isothermal+exterior model described above reproduces in detail our simulation results, where they overlap. As cooling of T_m^{iso} continues, increased ρ_χ^{iso} slows down further cooling, unlike the catastrophic collapse found in SIDM scenarios. The resulting density enhancement depends on how much the T_m^{iso} can cool over the age of the compact object t_{age} . We plot in Fig. 3 the final enhancement factor $\rho_\chi(R_\star)/\rho_\chi^\infty$ in the compact objects of Table I as a function of f and σ_m , for $\eta_{\text{eff}} = 1$. In the same figure, we delineate the regime where the subcomponent χ becomes the dominant DM, locally, inside the compact object, accounting for the fact that even the dominant, collisionless DM has an enhanced density due to gravitational focusing. By Liouville theorem, we can infer that

$\rho_{\text{CDM}}(R_*)/\rho_{\text{CDM}}^\infty \sim v_{\text{esc}}/\sqrt{T_m^\infty}$, which amounts to about 20(600) for WD(NS).

Next, we provide an analytical estimate for the order of magnitude of the final $\rho_\chi(R_*)$. Very crudely, we can approximate the numerator of the right hand side of Eq. (5) as $-\sigma_m r_{\text{iso}}^3 (\rho_\chi^\infty)^2 \left(\frac{T_m^{\text{iso}}}{T_m^\infty}\right)^{4\eta_{\text{eff}}-2} (T_m^{\text{iso}})^{3/2}$ and the denominator as $R_*^3 \rho_\chi^\infty \left(\frac{T_m^{\text{iso}}}{T_m^\infty}\right)^{2\eta_{\text{eff}}-1} e^{\frac{v_{\text{esc}}^2/2}{T_m^{\text{iso}}}} \left(\frac{v_{\text{esc}}^2/2}{T_m^{\text{iso}}}\right)$, assuming $\frac{\partial \ln \rho_\chi^{\text{iso}}}{\partial \ln T_m^{\text{iso}}} \approx -\frac{\Phi}{T_m^{\text{iso}}} \sim \frac{v_{\text{esc}}^2/2}{T_m^{\text{iso}}} \gg 3/2$ and the contributions from $r \sim R_*$ dominate the integral. The heat equation then reduces to

$$\frac{\dot{T}_m^{\text{iso}}}{T_m^{\text{iso}}} \sim \frac{1}{\tau_{\text{col}}^\infty} \left(\frac{v_{\text{esc}}^2}{2T_m^\infty}\right)^{2\eta_{\text{eff}}-\frac{1}{2}} \left(\frac{v_{\text{esc}}^2}{2T_m^{\text{iso}}}\right)^{\frac{5}{2}-2\eta_{\text{eff}}} e^{-\frac{v_{\text{esc}}^2}{2T_m^{\text{iso}}}} \quad (7)$$

where $\tau_{\text{col}}^\infty = (\rho_\chi^\infty \sigma_m \sqrt{T_m^\infty})^{-1}$. The final T_m^{iso} can be estimated by equating the above with $-t_{\text{age}}^{-1}$, and solving the resulting equation iteratively, giving $(v_{\text{esc}}^2/2)/T_m^{\text{iso}}|_{t=t_{\text{age}}} \approx \ln x + (5/2 - 2\eta_{\text{eff}}) \ln(\ln x)$, with $x = t_{\text{age}}/\tau_{\text{col}}^\infty$. For $\eta_{\text{eff}} = 1$, this yields

$$\begin{aligned} \frac{v_{\text{esc}}^2/2}{T_m^{\text{iso}}|_{t=t_{\text{age}}}} &\approx 20.4 + 3 \ln\left(\frac{v_{\text{esc}}}{0.02}\right) + \ln\left(\frac{f\sigma_m}{10^4 \text{ cm}^2/\text{g}}\right) \\ &= \begin{cases} 20.4 + \ln\left(\frac{f\sigma_m}{10^4 \text{ cm}^2/\text{g}}\right) & \text{(WD)} \\ 30.6 + \ln\left(\frac{f\sigma_m}{10^4 \text{ cm}^2/\text{g}}\right) & \text{(NS)} \end{cases} \quad (8) \end{aligned}$$

The corresponding ratio of the central density to the ambient density, given by Eq. 6, is

$$\begin{aligned} \frac{\rho_\chi(R_*)|_{t=t_{\text{age}}}}{\rho_\chi^\infty} &\sim 1 \times 10^9 \left(\frac{v_{\text{esc}}}{0.02}\right)^5 \left(\frac{f\sigma_m}{10^4 \text{ cm}^2/\text{g}}\right) \\ &= \begin{cases} 1 \times 10^9 \left(\frac{f\sigma_m}{10^4 \text{ cm}^2/\text{g}}\right) & \text{(WD)} \\ 2 \times 10^{16} \left(\frac{f\sigma_m}{10^4 \text{ cm}^2/\text{g}}\right) & \text{(NS)} \end{cases} \quad (9) \end{aligned}$$

These rough estimates are in agreement with the previously obtained results, displayed in Fig. 3, based on numerically solving Eq. (5). Since $\rho_\chi^\infty \propto f$, this translates to the final central density scaling as $\rho_\chi(R_*)|_{t=t_{\text{age}}} \propto f^2 \sigma_m$. Hence, in scenarios with multiple DM components, even those with extremely tiny f 's can accumulate to considerable levels if they have compensatingly large $\sigma_m \propto f^{-2}$.

The dependence of the final central density on the compact object enters through its $\rho_\chi(R_*)|_{t=t_{\text{age}}} \propto v_{\text{esc}}^5 t_{\text{age}}$ scaling, which explains how the $\rho_\chi(R_*)$ for NS is a factor of $\sim (0.02/0.6) = 2 \times 10^7$ higher than that for WD. The total captured mass is concentrated at $r \lesssim R_*$ where ρ_χ is exponentially enhanced. It can be estimated as $M_{\text{iso}} \sim (4\pi/3) R_*^3 \rho_\chi(R_*) \propto v_{\text{esc}}^5 R_*^3 t_{\text{age}}$. Compared to a WD, an NS has a much higher v_{esc} but much lower R_* . For the benchmark properties listed in Table I, this amounts to M_{iso} that is one order of magnitude smaller in NS than in WD. To further quantify the efficiency of gravothermal pile-up, we can also compute its effective capture

radius R_{cap} , defined by $\pi R_{\text{cap}}^2 = M_{\text{iso}}/(\rho_\chi^\infty \sqrt{T_m^\infty} t_{\text{age}})$. As an example, fixing $f = 10\%$ and $\sigma_m = 10^{10} \text{ cm}^2/\text{g}$, we find that for WD(NS) $M_{\text{iso}} \sim 10^{-17} M_\odot (10^{-18} M_\odot)$ and $R_{\text{cap}} \sim 6000 \text{ km} (500 \text{ km})$. The obtained M_{iso} 's are much larger than the total mass of the initial adiabatic cloud, which we estimate to be $M_{\text{ad}} \approx 4 \times 10^{-22} f M_\odot$. The R_{cap} values for the chosen parameters are about the geometrical radius R_* for WD and far exceeds R_* for NS.

Discussion.— We have shown how dark particles with a large, elastic, self-scattering cross sections comprising a tiny fraction of the dark matter in an environment with a velocity dispersion σ_v accumulate in gravitational wells with escape velocity $v_{\text{esc}} \gg \sigma_v$. The minimality of the requisite conditions for this process to occur suggests its ubiquitous relevance.

The σ_m values assumed in this study arise in many familiar particle-physics models. For instance, a scalar singlet [54–59] has a self-scattering $\sigma_m = 9\lambda^2/32\pi m^3 \sim 10^4 \lambda^2 \text{ cm}^2/\text{g}(m/\text{MeV})^{-3}$ that could be large for a perturbative quartic coupling λ if the mass m is small. In models of composite dark particles, including the dark analogues of glueballs [60–62], mesonic [63], baryonic, atomic [64–67], and molecular [65, 68] states [69, 70], large elastic σ_m 's arise naturally as a consequence of the particles' residual strong self-interactions, large geometric sizes, or the presence of light force-mediators. If the binding energy of one of these states is much greater than their typical kinetic energy, their collisions are mostly elastic. We discuss the simplest of these models, scalar singlet and dark atom, further in the Supplemental Material. Some of these models predict velocity-dependent cross-sections [48, 71, 72]. Our analysis could be straightforwardly generalized to such cases as well.

Apart from WDs and NSs in galaxies, many other combinations of small σ_v and large v_{esc} exist. Small velocity dispersions $\sigma_v \ll 10^{-3}$ can be found in Galaxy outskirts, dwarf galaxies⁵, or scenarios where the subcomponent forms a dark disk via inelastic processes [21, 22]. Other gravitational wells with $v_{\text{esc}} \gtrsim 10^{-3}$ include massive main-sequence (MS) stars and population III stars.⁶ Based on the fitting formulas in the Appendix of Ref. [75], the radius of MS star scales with its mass M_* as $R_* \propto M_*^{0.6}$, which translates to $v_{\text{esc}}^2 \propto M_*^{0.4}$. Long-range χ -baryon interactions could deepen the potential well of a baryonic object relative to gravity [76], potentially leading to substantial χ piles even around the Sun or the Earth. Similar piles may also form around macroscopic DM states [77–83].

⁵Subcomponent particles with sufficiently small mean free paths can be shielded from ram stripping in dwarf galaxies. The fact that gas-rich dwarf galaxies exist suggests that this outcome is possible [73, 74].

⁶Black holes have $v_{\text{esc}} = 1$ but their absorptive inner boundary conditions act as a central sink that hinders pile-up.

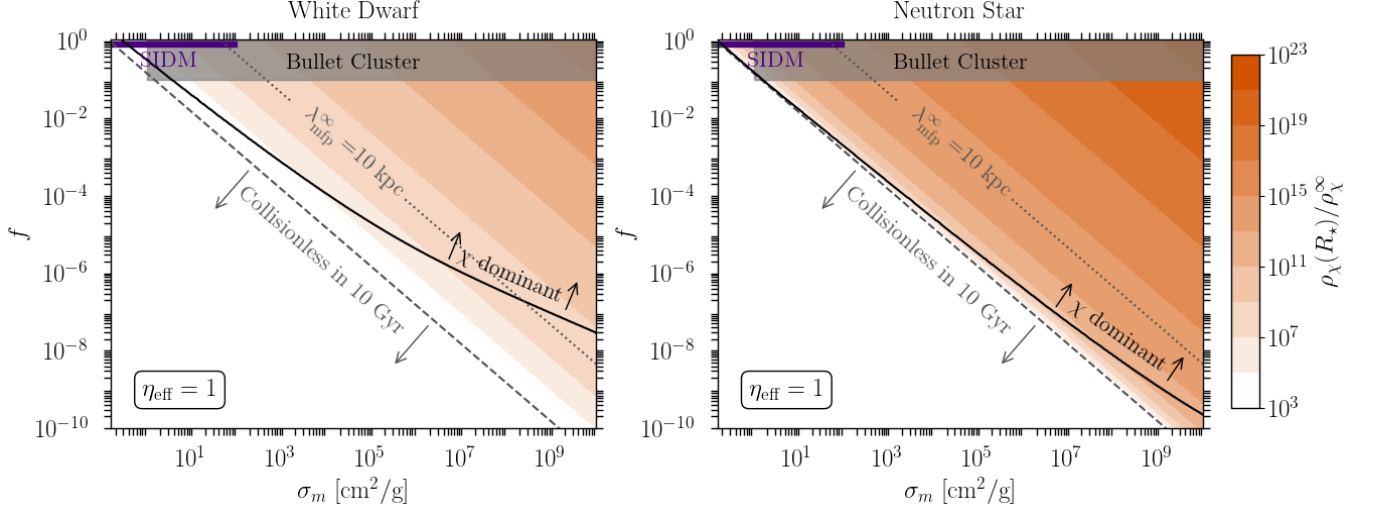


FIG. 3. Subcomponent χ parameter space. Here, f is χ 's galactic DM fraction, σ_m is χ 's cross-section-to-mass ratio, and $\rho_\chi(R_*)/\rho_\chi^\infty$ is χ 's final density-enhancement factor at the radius R_* of the central compact object: white dwarf (left) and neutron star (right). Regions of the parameter space ruled out by Bullet Cluster observations and favored by the SIDM paradigm are shown in gray and purple, respectively. Below the dashed lines, $\tau_{\text{col}} \gtrsim 10$ Gyr, and so the assumptions of the gravothermal formalism are not satisfied. Above the dotted lines, the ambient subcomponent behaves as a perfect fluid on galactic scales. The $\rho_\chi(R_*)/\rho_\chi^\infty$ are obtained by integrating Eq. (5) using Eq. (6) with $\eta_{\text{iso}} = \bar{\eta} = \eta_{\text{eff}} = 1$. Above the solid lines, the final central densities of the accumulated χ particles satisfy $\rho_\chi(R_*)/(0.4 \text{ GeV}/\text{cm}^3) \gtrsim 20$ (WD), 600 (NS), and thereby locally dominate over gravitationally focused cold collisionless DM inside the compact objects.

We have found that within the parameter space we considered, $f \lesssim 10\%$ and $\sigma_m \lesssim 10^{10} \text{ cm}^2/\text{g}$, a total captured mass of up to $10^{-17} M_\odot$ ($10^{-18} M_\odot$) for a WD(NS) in a typical galaxy is possible. Bigger χ piles can be achieved with $\sigma_m \gtrsim 10^{10} \text{ cm}^2/\text{g}$ and with more favorable combinations of R_* , v_{esc} , T_m^∞ , and ρ_χ^∞ , although we expect the total captured χ mass to be limited by the incoming χ flux to be less than $M_{\text{max}} = \rho_\chi^\infty \sqrt{T_m^\infty} \pi \lambda_{\text{grav}}^2 \times 10 \text{ Gyr} \sim 10^{-7} f M_\odot$ ($10^{-3} f M_\odot$) for a solar-mass object in a galaxy (dwarf galaxy). Measurably altering observable properties of compact objects typically requires percent-level or higher DM mass fraction [84–91]. Piles of χ around massive MS stars in dwarf galaxies, for instance, might be within the realm of detectability even in the simplest case with only gravity and χ self-scatterings.

In some cases, catastrophic outcomes are possible with much smaller captured mass. Depending on the model, when χ accumulates to sufficiently high central densities, various inelastic [92–95], number-changing [56, 96–98], or quantum-statistics [98–104] effects may turn on. The pile may also become self-gravitating [96, 101, 103, 105–109]. In the presence of χ -baryon coupling, χ particles in the pile may exchange energy with of the compact object through scatterings, potentially causing them to sink even deeper [110–113] and causing extra cooling or heating the compact object [84, 114]. Sufficiently light χ could be sourced by stellar cores, likely with collective dynamics and nontrivial interplay with the captured χ [115, 116]. The gravitational accumulation mechanism

studied here could be a precursor or a contributing effect to the scenarios studied in [78, 98–103, 117–119].

If the χ particles annihilate into final states that include SM particles escaping the compact object, the resulting indirect-detection signals could be significantly enhanced due to the n_χ^2 dependence of the annihilation rate and the concentrated density of χ around compact stars [120, 121]. Details of the resulting photon flux are, of course, model-dependent. For now, we can compute part of the J -factor $J(r) \propto \int_0^r 4\pi r'^2 dr' (\rho_\chi^{\text{iso}})^2$, which is independent of the microphysics of χ . In a region where the typical separation between compact objects is 0.1 pc, the annihilation signal from χ inside compact objects is stronger than that of the ambient χ if the J -factor ratio $J(R_*)/J(1 \text{ pc}) \sim (R_*/\text{pc})^3 [\rho_\chi(R_*)/\rho_\chi^\infty]^2$ is greater than unity, which amounts to $\rho_\chi(R_*)/\rho_\chi^\infty \gtrsim 10^{13}$ (10^{17}) for WD (NS). Density enhancements at those levels are achievable for sufficiently large $f^2 \sigma_m$. Decay signals would not have enhanced strengths on average, but would have different morphologies [23], if the telescope could resolve them.

Therefore, through gravothermal pile-up even a tiny subcomponent of dark matter can leave observable signatures. We defer detailed investigation of these signals to separate work.

Acknowledgments.— We thank Abhishek Banerjee for early collaboration, and Peter Graham and David E. Kaplan for useful conversations. R.E. is supported by the Grant 63034 from the John Templeton Foundation and the University of Maryland Quantum Technology Center. E.H.T. acknowledges support by NSF Grant PHY-2310429, Simons Investigator Award No. 824870, the Gordon and Betty Moore Foundation Grant GBMF7946, and the U.S. Department of Energy (DOE), Office of Science, National Quantum Information Science Research Centers, Superconducting Quantum Materials and Systems Center (SQMS) under contract No. DEAC02-07CH11359.

* ebadi@umd.edu

† ehtanin@stanford.edu

- [1] A. H. G. Peter, M. Rocha, J. S. Bullock, and M. Kaplinghat, *Mon. Not. Roy. Astron. Soc.* **430**, 105 (2013), [arXiv:1208.3026 \[astro-ph.CO\]](#).
- [2] S. W. Randall, M. Markevitch, D. Clowe, A. H. Gonzalez, and M. Bradac, *Astrophys. J.* **679**, 1173 (2008), [arXiv:0704.0261 \[astro-ph\]](#).
- [3] M. Markevitch, A. H. Gonzalez, D. Clowe, A. Vikhlinin, L. David, W. Forman, C. Jones, S. Murray, and W. Tucker, *Astrophys. J.* **606**, 819 (2004), [arXiv:astro-ph/0309303](#).
- [4] D. N. Spergel and P. J. Steinhardt, *Phys. Rev. Lett.* **84**, 3760 (2000), [arXiv:astro-ph/9909386](#).
- [5] S. Tulin and H.-B. Yu, *Phys. Rept.* **730**, 1 (2018), [arXiv:1705.02358 \[hep-ph\]](#).
- [6] M. Kaplinghat, T. Ren, and H.-B. Yu, *JCAP* **06**, 027 (2020), [arXiv:1911.00544 \[astro-ph.GA\]](#).
- [7] J. S. Bullock and M. Boylan-Kolchin, *Ann. Rev. Astron. Astrophys.* **55**, 343 (2017), [arXiv:1707.04256 \[astro-ph.CO\]](#).
- [8] S. Garrison-Kimmel, P. F. Hopkins, A. Wetzel, J. S. Bullock, M. Boylan-Kolchin, D. Kereš, C.-A. Faucher-Giguère, K. El-Badry, A. Lamberts, E. Quataert, and R. Sanderson, *MNRAS* **487**, 1380 (2019), [arXiv:1806.04143 \[astro-ph.GA\]](#).
- [9] J. Pollack, D. N. Spergel, and P. J. Steinhardt, *Astrophys. J.* **804**, 131 (2015), [arXiv:1501.00017 \[astro-ph.CO\]](#).
- [10] M. G. Roberts, L. Braff, A. Garg, S. Profumo, T. Jeltema, and J. O'Donnell, *JCAP* **01**, 060 (2025), [arXiv:2410.17480 \[astro-ph.GA\]](#).
- [11] J. Choquette, J. M. Cline, and J. M. Cornell, *JCAP* **07**, 036 (2019), [arXiv:1812.05088 \[astro-ph.CO\]](#).
- [12] R. N. Mohapatra, S. Nussinov, and V. L. Teplitz, *Phys. Rev. D* **66**, 063002 (2002), [arXiv:hep-ph/0111381](#).
- [13] R. Foot and S. Vagnozzi, *Phys. Rev. D* **91**, 023512 (2015), [arXiv:1409.7174 \[hep-ph\]](#).
- [14] Z. Chacko, H.-S. Goh, and R. Harnik, *Phys. Rev. Lett.* **96**, 231802 (2006), [arXiv:hep-ph/0506256](#).
- [15] Z. Chacko, Y. Nomura, M. Papucci, and G. Perez, *JHEP* **01**, 126 (2006), [arXiv:hep-ph/0510273](#).
- [16] L. B. Okun, *Phys. Usp.* **50**, 380 (2007), [arXiv:hep-ph/0606202](#).
- [17] Z. Berezhiani, *Int. J. Mod. Phys. A* **19**, 3775 (2004), [arXiv:hep-ph/0312335](#).
- [18] R. Foot, *Int. J. Mod. Phys. A* **29**, 1430013 (2014), [arXiv:1401.3965 \[astro-ph.CO\]](#).
- [19] R. Foot, *Int. J. Mod. Phys. D* **13**, 2161 (2004), [arXiv:astro-ph/0407623](#).
- [20] P. Ciarcelluti, *Int. J. Mod. Phys. D* **19**, 2151 (2010), [arXiv:1102.5530 \[astro-ph.CO\]](#).
- [21] J. Fan, A. Katz, L. Randall, and M. Reece, *Phys. Dark Univ.* **2**, 139 (2013), [arXiv:1303.1521 \[astro-ph.CO\]](#).
- [22] J. Fan, A. Katz, L. Randall, and M. Reece, *Phys. Rev. Lett.* **110**, 211302 (2013), [arXiv:1303.3271 \[hep-ph\]](#).
- [23] P. Agrawal and L. Randall, *JCAP* **12**, 019 (2017), [arXiv:1706.04195 \[hep-ph\]](#).
- [24] Z. Chacko, Y. Cui, S. Hong, T. Okui, and Y. Tsai, *JHEP* **12**, 108 (2016), [arXiv:1609.03569 \[astro-ph.CO\]](#).
- [25] F.-Y. Cyr-Racine, R. de Putter, A. Raccanelli, and K. Sigurdson, *Phys. Rev. D* **89**, 063517 (2014), [arXiv:1310.3278 \[astro-ph.CO\]](#).
- [26] M. R. Buckley and A. DiFranzo, *Phys. Rev. Lett.* **120**, 051102 (2018), [arXiv:1707.03829 \[hep-ph\]](#).
- [27] A. Ghalsasi and M. McQuinn, *Phys. Rev. D* **97**, 123018 (2018), [arXiv:1712.04779 \[astro-ph.GA\]](#).
- [28] J. H. Chang, D. Egana-Ugrinovic, R. Essig, and C. Kouvaris, *JCAP* **03**, 036 (2019), [arXiv:1812.07000 \[hep-ph\]](#).
- [29] S. Roy, X. Shen, J. Barron, M. Lisanti, D. Curtin, N. Murray, and P. F. Hopkins, *Astrophys. J.* **982**, 175 (2025), [arXiv:2408.15317 \[astro-ph.GA\]](#).
- [30] C. Gemmell, S. Roy, X. Shen, D. Curtin, M. Lisanti, N. Murray, and P. F. Hopkins, *Astrophys. J.* **967**, 21 (2024), [arXiv:2311.02148 \[astro-ph.GA\]](#).
- [31] S. Roy, X. Shen, M. Lisanti, D. Curtin, N. Murray, and P. F. Hopkins, *Astrophys. J. Lett.* **954**, L40 (2023), [arXiv:2304.09878 \[astro-ph.GA\]](#).
- [32] M. Geller and Z. Heller-Algazi, *JHEP* **03**, 184 (2023), [arXiv:2210.03126 \[hep-ph\]](#).
- [33] Z. Chacko, D. Curtin, M. Geller, and Y. Tsai, *JHEP* **11**, 198 (2021), [arXiv:2104.02074 \[hep-ph\]](#).
- [34] R. N. Mohapatra and V. L. Teplitz, *Astrophys. J.* **478**, 29 (1997), [arXiv:astro-ph/9603049](#).
- [35] R. A. Crain, V. R. Eke, C. S. Frenk, A. Jenkins, I. G. McCarthy, J. F. Navarro, and F. R. Pearce, *Mon. Not. Roy. Astron. Soc.* **377**, 41 (2007), [arXiv:astro-ph/0610602](#).
- [36] H. Zheng, S. Bose, C. S. Frenk, L. Gao, A. Jenkins, S. Liao, V. Springel, J. Wang, and S. D. M. White, *Mon. Not. Roy. Astron. Soc.* **532**, 3151 (2024), [arXiv:2403.17044 \[astro-ph.GA\]](#).
- [37] B. Moore, S. Gelato, A. Jenkins, F. R. Pearce, and V. Quilis, *Astrophys. J. Lett.* **535**, L21 (2000), [arXiv:astro-ph/0002308](#).
- [38] N. Yoshida, V. Springel, S. D. M. White, and G. Tormen, *Astrophys. J. Lett.* **535**, L103 (2000), [arXiv:astro-ph/0002362](#).
- [39] E. Bertschinger, *ApJS* **58**, 39 (1985).
- [40] D. Lynden-Bell and P. P. Eggleton, *MNRAS* **191**, 483 (1980).
- [41] S. Balberg, S. L. Shapiro, and S. Inagaki, *Astrophys. J.* **568**, 475 (2002), [arXiv:astro-ph/0110561](#).
- [42] S. L. Shapiro, *Phys. Rev. D* **98**, 023021 (2018), [arXiv:1809.02618 \[astro-ph.HE\]](#).
- [43] K.-J. Ahn and P. R. Shapiro, *Mon. Not. Roy. Astron. Soc.* **363**, 1092 (2005), [arXiv:astro-ph/0412169](#).

- [44] J. Koda and P. R. Shapiro, *MNRAS* **415**, 1125 (2011), [arXiv:1101.3097 \[astro-ph.CO\]](#).
- [45] S. Yang, X. Du, Z. C. Zeng, A. Benson, F. Jiang, E. O. Nadler, and A. H. G. Peter, *Astrophys. J.* **946**, 47 (2023), [arXiv:2205.02957 \[astro-ph.CO\]](#).
- [46] C. Mace, S. Yang, Z. Carton Zeng, A. H. G. Peter, X. Du, and A. Benson, *arXiv e-prints*, [arXiv:2504.13004 \(2025\)](#), [arXiv:2504.13004 \[astro-ph.GA\]](#).
- [47] H. Nishikawa, K. K. Boddy, and M. Kaplinghat, *Phys. Rev. D* **101**, 063009 (2020), [arXiv:1901.00499 \[astro-ph.GA\]](#).
- [48] N. J. Outmezguine, K. K. Boddy, S. Gad-Nasr, M. Kaplinghat, and L. Sagunski, *Mon. Not. Roy. Astron. Soc.* **523**, 4786 (2023), [arXiv:2204.06568 \[astro-ph.GA\]](#).
- [49] S. Gad-Nasr, K. K. Boddy, M. Kaplinghat, N. J. Outmezguine, and L. Sagunski, *JCAP* **05**, 131 (2024), [arXiv:2312.09296 \[astro-ph.GA\]](#).
- [50] K. Boddy, H. Nishikawa, S. Gad-Nasr, and L. Sagunski, “GravothermalSIDM,” <https://github.com/kboddy/GravothermalSIDM>, accessed: 2025-05-19.
- [51] S. L. Shapiro and V. Paschalidis, *Phys. Rev. D* **89**, 023506 (2014), [arXiv:1402.0005 \[astro-ph.CO\]](#).
- [52] P. Amaro-Seoane, M. Freitag, and R. Spurzem, *Mon. Not. Roy. Astron. Soc.* **352**, 655 (2004), [arXiv:astro-ph/0401163](#).
- [53] J. N. Bahcall and R. A. Wolf, *Astrophys. J.* **209**, 214 (1976).
- [54] J. McDonald, *Phys. Rev. Lett.* **88**, 091304 (2002), [arXiv:hep-ph/0106249](#).
- [55] M. Heikinheimo, T. Tenkanen, K. Tuominen, and V. Vaskonen, *Phys. Rev. D* **94**, 063506 (2016), [Erratum: *Phys. Rev. D* **96**, 109902 (2017)], [arXiv:1604.02401 \[astro-ph.CO\]](#).
- [56] Y. Hochberg, E. Kuflik, T. Volansky, and J. G. Wacker, *Phys. Rev. Lett.* **113**, 171301 (2014), [arXiv:1402.5143 \[hep-ph\]](#).
- [57] C. P. Burgess, M. Pospelov, and T. ter Veldhuis, *Nucl. Phys. B* **619**, 709 (2001), [arXiv:hep-ph/0011335](#).
- [58] N. Bernal, M. Heikinheimo, T. Tenkanen, K. Tuominen, and V. Vaskonen, *Int. J. Mod. Phys. A* **32**, 1730023 (2017), [arXiv:1706.07442 \[hep-ph\]](#).
- [59] J. H. Chang, M. O. Olea-Romacho, and E. H. Tanin, *Phys. Rev. D* **106**, 113003 (2022), [arXiv:2210.05680 \[hep-ph\]](#).
- [60] K. K. Boddy, J. L. Feng, M. Kaplinghat, and T. M. P. Tait, *Phys. Rev. D* **89**, 115017 (2014), [arXiv:1402.3629 \[hep-ph\]](#).
- [61] B. Jo, H. Kim, H. D. Kim, and C. S. Shin, *Phys. Rev. D* **103**, 083528 (2021), [arXiv:2010.10880 \[hep-ph\]](#).
- [62] A. Soni and Y. Zhang, *Phys. Rev. D* **93**, 115025 (2016), [arXiv:1602.00714 \[hep-ph\]](#).
- [63] S. Bhattacharya, B. Melić, and J. Wudka, *JHEP* **02**, 115 (2014), [arXiv:1307.2647 \[hep-ph\]](#).
- [64] D. E. Kaplan, G. Z. Krnjaic, K. R. Rehermann, and C. M. Wells, *JCAP* **05**, 021 (2010), [arXiv:0909.0753 \[hep-ph\]](#).
- [65] J. M. Cline, Z. Liu, G. Moore, and W. Xue, *Phys. Rev. D* **89**, 043514 (2014), [arXiv:1311.6468 \[hep-ph\]](#).
- [66] F.-Y. Cyr-Racine and K. Sigurdson, *Phys. Rev. D* **87**, 103515 (2013), [arXiv:1209.5752 \[astro-ph.CO\]](#).
- [67] K. K. Boddy, M. Kaplinghat, A. Kwa, and A. H. G. Peter, *Phys. Rev. D* **94**, 123017 (2016), [arXiv:1609.03592 \[hep-ph\]](#).
- [68] M. Ryan, J. Gurian, S. Shandera, and D. Jeong, *Astrophys. J.* **934**, 120 (2022), [arXiv:2106.13245 \[astro-ph.CO\]](#).
- [69] J. M. Cline, Z. Liu, G. D. Moore, and W. Xue, *Phys. Rev. D* **90**, 015023 (2014), [arXiv:1312.3325 \[hep-ph\]](#).
- [70] G. D. Kribs and E. T. Neil, *Int. J. Mod. Phys. A* **31**, 1643004 (2016), [arXiv:1604.04627 \[hep-ph\]](#).
- [71] M. Kaplinghat, S. Tulin, and H.-B. Yu, *Phys. Rev. Lett.* **116**, 041302 (2016), [arXiv:1508.03339 \[astro-ph.CO\]](#).
- [72] P. Agrawal, F.-Y. Cyr-Racine, L. Randall, and J. Scholtz, *JCAP* **05**, 022 (2017), [arXiv:1610.04611 \[hep-ph\]](#).
- [73] M. E. Putman, Y. Zheng, A. M. Price-Whelan, J. Grcevich, A. C. Johnson, E. Tollerud, and J. E. G. Peek, *ApJ* **913**, 53 (2021), [arXiv:2101.07809 \[astro-ph.GA\]](#).
- [74] J. Grcevich and M. E. Putman, *ApJ* **696**, 385 (2009), [arXiv:0901.4975 \[astro-ph.GA\]](#).
- [75] N. H. Nguyen, E. H. Tanin, and M. Kamionkowski, *JCAP* **11**, 091 (2023), [arXiv:2307.11216 \[hep-ph\]](#).
- [76] Z. Bogorad, P. W. Graham, and H. Ramani, *JCAP* **04**, 006 (2025), [arXiv:2410.07324 \[hep-ph\]](#).
- [77] D. M. Jacobs, G. D. Starkman, and B. W. Lynn, *Mon. Not. Roy. Astron. Soc.* **450**, 3418 (2015), [arXiv:1410.2236 \[astro-ph.CO\]](#).
- [78] Y. Bai, A. J. Long, and S. Lu, *JCAP* **09**, 044 (2020), [arXiv:2003.13182 \[astro-ph.CO\]](#).
- [79] L. Tolos, J. Schaffner-Bielich, and Y. Dengler, *Phys. Rev. D* **92**, 123002 (2015), [Erratum: *Phys. Rev. D* **103**, 109901 (2021)], [arXiv:1507.08197 \[astro-ph.HE\]](#).
- [80] D. M. Grabowska, T. Melia, and S. Rajendran, *Phys. Rev. D* **98**, 115020 (2018), [arXiv:1807.03788 \[hep-ph\]](#).
- [81] D. E. Kaplan, X. Luo, N. H. Nguyen, S. Rajendran, and E. H. Tanin, *Phys. Rev. D* **111**, 023041 (2025), [arXiv:2407.06262 \[hep-ph\]](#).
- [82] M. A. Fedderke, D. E. Kaplan, A. Mathur, S. Rajendran, and E. H. Tanin, *Phys. Rev. D* **109**, 123028 (2024), [arXiv:2402.15581 \[hep-ph\]](#).
- [83] R. Ebadi *et al.*, *Phys. Rev. D* **104**, 015041 (2021), [arXiv:2105.03998 \[hep-ph\]](#).
- [84] G. Bertone and M. Fairbairn, *Phys. Rev. D* **77**, 043515 (2008), [arXiv:0709.1485 \[astro-ph\]](#).
- [85] M. Deliyergiyev, A. Del Popolo, L. Tolos, M. Le Delliou, X. Lee, and F. Burgio, *Phys. Rev. D* **99**, 063015 (2019), [arXiv:1903.01183 \[gr-qc\]](#).
- [86] F. Sandin and P. Ciarelluti, *Astropart. Phys.* **32**, 278 (2009), [arXiv:0809.2942 \[astro-ph\]](#).
- [87] J. Ellis, A. Hektor, G. Hütsi, K. Kannike, L. Marzola, M. Raidal, and V. Vaskonen, *Phys. Lett. B* **781**, 607 (2018), [arXiv:1710.05540 \[astro-ph.CO\]](#).
- [88] H. Koehn, E. Giangrandi, N. Kunert, R. Somasundaram, V. Sagun, and T. Dietrich, *Phys. Rev. D* **110**, 103033 (2024), [arXiv:2408.14711 \[astro-ph.HE\]](#).
- [89] D. R. Karkevandi, S. Shakeri, V. Sagun, and O. Ivanytskyi, *Phys. Rev. D* **105**, 023001 (2022), [arXiv:2109.03801 \[astro-ph.HE\]](#).
- [90] K.-L. Leung, M.-c. Chu, and L.-M. Lin, *Phys. Rev. D* **105**, 123010 (2022), [arXiv:2207.02433 \[astro-ph.HE\]](#).
- [91] E. Giangrandi, V. Sagun, O. Ivanytskyi, C. Providência, and T. Dietrich, *Astrophys. J.* **953**, 115 (2023), [arXiv:2209.10905 \[astro-ph.HE\]](#).
- [92] L. Pearce and A. Kusenko, *Phys. Rev. D* **87**, 123531 (2013), [arXiv:1303.7294 \[hep-ph\]](#).

- [93] M. Cirelli, P. Panci, K. Petraki, F. Sala, and M. Taoso, *JCAP* **05**, 036 (2017), [arXiv:1612.07295 \[hep-ph\]](#).
- [94] L. Pearce, K. Petraki, and A. Kusenko, *Phys. Rev. D* **91**, 083532 (2015), [arXiv:1502.01755 \[hep-ph\]](#).
- [95] K. Freese, T. Rindler-Daller, D. Spolyar, and M. Valluri, *Rept. Prog. Phys.* **79**, 066902 (2016), [arXiv:1501.02394 \[astro-ph.CO\]](#).
- [96] N. F. Bell, A. Melatos, and K. Petraki, *Phys. Rev. D* **87**, 123507 (2013), [arXiv:1301.6811 \[hep-ph\]](#).
- [97] D. Pappadopulo, J. T. Ruderman, and G. Trevisan, *Phys. Rev. D* **94**, 035005 (2016), [arXiv:1602.04219 \[hep-ph\]](#).
- [98] P. Ralegankar, D. Perri, and T. Kobayashi, (2024), [arXiv:2410.18948 \[astro-ph.CO\]](#).
- [99] D. Budker, J. Eby, M. Gorghetto, M. Jiang, and G. Perez, *JCAP* **12**, 021 (2023), [arXiv:2306.12477 \[hep-ph\]](#).
- [100] J. Eby, C. Kouvaris, N. G. Nielsen, and L. C. R. Wijewardhana, *JHEP* **02**, 028 (2016), [arXiv:1511.04474 \[hep-ph\]](#).
- [101] J. Bramante, K. Fukushima, and J. Kumar, *Phys. Rev. D* **87**, 055012 (2013), [arXiv:1301.0036 \[hep-ph\]](#).
- [102] C. Kouvaris and P. Tinyakov, *Phys. Rev. Lett.* **107**, 091301 (2011), [arXiv:1104.0382 \[astro-ph.CO\]](#).
- [103] S. D. McDermott, H.-B. Yu, and K. M. Zurek, *Phys. Rev. D* **85**, 023519 (2012), [arXiv:1103.5472 \[hep-ph\]](#).
- [104] B. Bertoni, A. E. Nelson, and S. Reddy, *Phys. Rev. D* **88**, 123505 (2013), [arXiv:1309.1721 \[hep-ph\]](#).
- [105] I. Goldman and S. Nussinov, *Phys. Rev. D* **40**, 3221 (1989).
- [106] A. Gould, B. T. Draine, R. W. Romani, and S. Nussinov, *Phys. Lett. B* **238**, 337 (1990).
- [107] J. Bramante, T. Linden, and Y.-D. Tsai, *Phys. Rev. D* **97**, 055016 (2018), [arXiv:1706.00001 \[hep-ph\]](#).
- [108] B. Dasgupta, R. Laha, and A. Ray, *Phys. Rev. Lett.* **126**, 141105 (2021), [arXiv:2009.01825 \[astro-ph.HE\]](#).
- [109] R. Garani, Y. Genolini, and T. Hambye, *JCAP* **05**, 035 (2019), [arXiv:1812.08773 \[hep-ph\]](#).
- [110] T. Güver, A. E. Erkoca, M. Hall Reno, and I. Sarcevic, *JCAP* **05**, 013 (2014), [arXiv:1201.2400 \[hep-ph\]](#).
- [111] N. F. Bell, G. Busoni, M. E. Ramirez-Quezada, S. Robles, and M. Virgato, *JCAP* **10**, 083 (2021), [arXiv:2104.14367 \[hep-ph\]](#).
- [112] B. Dasgupta, A. Gupta, and A. Ray, *JCAP* **08**, 018 (2019), [arXiv:1906.04204 \[hep-ph\]](#).
- [113] B. Dasgupta, A. Gupta, and A. Ray, *JCAP* **10**, 023 (2020), [arXiv:2006.10773 \[hep-ph\]](#).
- [114] C. Kouvaris, *Phys. Rev. D* **77**, 023006 (2008), [arXiv:0708.2362 \[astro-ph\]](#).
- [115] J. H. Chang, D. E. Kaplan, S. Rajendran, H. Ramani, and E. H. Tanin, *Phys. Rev. Lett.* **129**, 211101 (2022), [arXiv:2205.11527 \[hep-ph\]](#).
- [116] A. Berlin, S. Rajendran, H. Ramani, and E. H. Tanin, *JHEP* **04**, 198 (2025), [arXiv:2412.03643 \[hep-ph\]](#).
- [117] Y. Wu, S. Baum, K. Freese, L. Visinelli, and H.-B. Yu, *Phys. Rev. D* **106**, 043028 (2022), [arXiv:2205.10904 \[hep-ph\]](#).
- [118] Y. Bai, V. Barger, and J. Berger, *JHEP* **12**, 127 (2016), [arXiv:1612.00438 \[hep-ph\]](#).
- [119] I. Armstrong, B. Gurbuz, D. Curtin, and C. D. Matzner, *Astrophys. J.* **965**, 42 (2024), [arXiv:2311.18086 \[astro-ph.HE\]](#).
- [120] R. K. Leane, T. Linden, P. Mukhopadhyay, and N. Toro, *Phys. Rev. D* **103**, 075030 (2021), [arXiv:2101.12213 \[astro-ph.HE\]](#).
- [121] T. T. Q. Nguyen and T. M. P. Tait, *Phys. Rev. D* **107**, 115016 (2023), [arXiv:2212.12547 \[hep-ph\]](#).
- [122] V. M. Sabarish, M. Brüggen, K. Schmidt-Hoberg, and M. S. Fischer, (2025), [arXiv:2505.14779 \[astro-ph.CO\]](#).
- [123] K. Petraki and R. R. Volkas, *Int. J. Mod. Phys. A* **28**, 1330028 (2013), [arXiv:1305.4939 \[hep-ph\]](#).
- [124] D. E. Kaplan, M. A. Luty, and K. M. Zurek, *Phys. Rev. D* **79**, 115016 (2009), [arXiv:0901.4117 \[hep-ph\]](#).
- [125] Z. G. Berezhiani, A. D. Dolgov, and R. N. Mohapatra, *Phys. Lett. B* **375**, 26 (1996), [arXiv:hep-ph/9511221](#).
- [126] P. Adshead, Y. Cui, and J. Shelton, *JHEP* **06**, 016 (2016), [arXiv:1604.02458 \[hep-ph\]](#).
- [127] T. Tenkanen, *Phys. Rev. Lett.* **123**, 061302 (2019), [arXiv:1905.01214 \[astro-ph.CO\]](#).
- [128] P. J. E. Peebles and A. Vilenkin, *Phys. Rev. D* **60**, 103506 (1999), [arXiv:astro-ph/9904396](#).
- [129] E. W. Kolb and A. J. Long, *Rev. Mod. Phys.* **96**, 045005 (2024), [arXiv:2312.09042 \[astro-ph.CO\]](#).
- [130] O. Lebedev, *Prog. Part. Nucl. Phys.* **120**, 103881 (2021), [arXiv:2104.03342 \[hep-ph\]](#).
- [131] J. M. Cline, K. Kainulainen, P. Scott, and C. Weniger, *Phys. Rev. D* **88**, 055025 (2013), [Erratum: *Phys. Rev. D* **92**, 039906 (2015)], [arXiv:1306.4710 \[hep-ph\]](#).

Supplemental Material

Making the Subdominant Dominant: Gravothermal Pile-Up of Collisional Dark Matter Around Compact Objects

Reza Ebadi and Erwin H. Tanin

GRAVOTHERMAL FLUID FORMALISM

Our setup consists of a gravitational potential well and a thermal fluid, denoted here by subscripts ‘pot’ and χ , respectively, to prevent ambiguity in notation when necessary. We focus on a parameter space where the self-gravity of the fluid can be neglected. The gravothermal set of equations can be written as

$$\text{Hydrostatic equilibrium:} \quad \partial_r(\rho_\chi T_m) = -\frac{GM_{\text{pot}}(r)}{r^2} \rho_\chi \quad (\text{S1})$$

$$\text{Energy flux:} \quad \frac{L}{4\pi r^2} = -\kappa_{\text{eff}} \partial_r T_m \quad (\text{S2})$$

$$\text{1st law of thermodynamics:} \quad \partial_r L = -4\pi r^2 \rho_\chi T_m \partial_t \left(\ln \frac{T_m^{3/2}}{\rho_\chi} \right) \quad (\text{S3})$$

where $M_{\text{pot}}(r)$ is the mass enclosed within a sphere of radius r , T_m is the temperature *per unit mass* of the fluid, and L is the outward heat-conduction luminosity.

The effective conductivity κ_{eff} captures both the short mean free path (SMFP) and long mean free path (LMFP) regimes, as well as interpolating between the two:

$$\kappa_{\text{eff}} = \left(\kappa_{\text{smfp}}^{-1} + \kappa_{\text{lmfp}}^{-1} \right)^{-1} \quad (\text{S4})$$

where

$$\kappa_{\text{smfp}} = \frac{3}{2} \rho_\chi C_{\text{smfp}} \frac{\lambda_{\text{mfp}}^2}{\tau_{\text{col}}}, \quad \kappa_{\text{lmfp}} = \frac{3}{2} \rho_\chi C_{\text{lmfp}} \frac{H^2}{\tau_{\text{col}}} \quad (\text{S5})$$

The numerical factors $C_{\text{smfp}} = b/a = 25\pi^2/168$ and $C_{\text{lmfp}} = 0.753$ are $\mathcal{O}(1)$. C_{smfp} can be derived from first principles, whereas C_{lmfp} is obtained by fitting numerical results such that κ_{eff} gives acceptable results in the interpolation regime [S43–S46]. In the SMFP regime, the relevant length scale is the distance between successive collisions, $\lambda_{\text{mfp}} = 1/(\rho_\chi \sigma_m)$. In the LMFP regime, each particle completes multiple orbits between collisions, during which the order of magnitude of the change in its radial position is given by $H \sim v_r t_{\text{orbit}}$ [S122]. Here, $v_r \simeq \sqrt{T_m}$ is radial velocity dispersion, and t_{orbit} is orbital timescale. Outside the gravitational potential of a star $v_r \sim \sqrt{GM_\star/r}$ and $t_{\text{orbit}} \sim \sqrt{r^3/GM_\star}$, while inside the star $v_r \sim \sqrt{GM_\star(3R_\star^2 - r^2)/2R_\star^3}$ and $t_{\text{orbit}} \sim \sqrt{R_\star^3/GM_\star}$. In both cases, we assumed that the virial theorem holds, as justified by the long mean free path ($\lambda_{\text{mfp}} \gg H$). We find $H \sim r$ (as in [S42, S51]) as long as r is not much smaller than R_\star . This length scale is consistent with the definition of the gravitational scale height: the characteristic distance over which the thermodynamic properties of the system change significantly due to the gravitational potential, i.e., $H \partial_r \Phi \sim T_m$. Which also implies, $H \sim \Phi/\partial_r \Phi \sim r$.

Gravothermal evolution. In the parameter space relevant to the current work, the system begins in the LMFP regime (characterized by high temperature and low density) and undergoes gravothermal evolution (leading to lower temperatures and higher densities). This evolution naturally drives the system from the LMFP regime to the SMFP regime. In either of the limiting cases, deep LMFP or deep SMFP, one of the corresponding conductivities becomes small and thus dominates the total effective conductivity, resulting in inefficient heat transport. However, near the transition boundary between the two regimes, both conductivities are comparable and larger than in either limit. Consequently, the gravothermal evolution is the fastest near this boundary, a regime we dub the intermediate mean free path (IMFP) regime. The transition happens when

$$\rho_\chi^{\text{imfp}} \simeq \sqrt{\frac{C_{\text{smfp}}}{C_{\text{lmfp}}}} \frac{1}{r \sigma_m} \quad (\text{S6})$$

The gravothermal fluid formalism is based on Fourier’s law of thermal conduction, namely Eq. (S2). Fundamentally, the latter is a concept that is derived from an expansion of the energy-momentum tensor of a near-perfect fluid to

first order in the MFP. In order for the expansion to make sense, strictly speaking the MFP must be tiny compared to other length scales of the problem, i.e. in the SMFP region. However, the situation in the LMFP regime is not as severe as it naively seems. In the LMFP case, the effective MFP is set by the gravitational scale height instead of the collisional MFP. The former is typically of the same order as r , which sets the fractional gradients of many quantities. So the small MFP expansion is at the very least marginally justified. In fact, it has been shown that if the prefactor of the conductivity is properly calibrated, the fluid formalism can produce results that agree well with that of N-body simulations even in the LMFP limit [S43–S46].

HYDRODYNAMICAL SIMULATIONS OF GRAVOTHERMAL EVOLUTION

We use the method developed in [S9] and adapted by [S47–S49] (codebase available at [S50]) to solve the set of gravothermal fluid equations, Eqs. (S1), (S2), & (S3). For a description of the numerical implementation, see Appendix A of [S47]. A high-level summary of the workflow is as follows:

- *Divide the fluid into spherically symmetric shells:* The fluid is discretized into multiple concentric shells. Each shell has a fixed mass throughout evolution.
- *Heat conduction step:* Small amount of heat transfer occurs between neighboring shells. The time step used is much shorter than the collisional timescale τ_{col} . This process slightly perturbs hydrostatic equilibrium.
- *Hydrostatic adjustment steps:* Following the heat conduction, the system is driven back toward hydrostatic equilibrium. This is done through multiple adjustment steps during which the positions, pressures, and densities of the shells are updated iteratively. This process conserves entropy.

Dimensionless Quantities and Equations

The gravothermal fluid equations involve a set of six physical quantities: $\{r, M_{\text{pot}}, \rho_\chi, T_m \text{ (or } v_\chi), t, \sigma_m, L\}$. To convert the gravothermal fluid equations into a dimensionless form (denoted by tilde), four constraints must be imposed on the scaling quantities (denoted by the subscript 0). Note that the energy flux equation contributes two of these constraints due to the presence of both LMFP and SMFP conductivity regimes. This leaves three degrees of freedom to choose independent scaling quantities. We select $\{M_0, r_0, \rho_0\}$. Other parameters of interest can be made dimensionless through suitable combinations of these three scaling quantities:

$$T_0 = v_0^2 = \frac{GM_0}{r_0} \quad (\text{S7})$$

$$\sigma_0 = \frac{1}{\rho_0 r_0} \quad (\text{S8})$$

$$L_0 = \frac{4\pi\rho_0 v_0^2 r_0^3}{t_0} \quad (\text{S9})$$

$$t_0 = \frac{1}{a\sigma_m \rho_0 v_0} \quad (\text{S10})$$

$$\Phi_0 = v_0^2 \quad (\text{S11})$$

where $a = 4/\sqrt{\pi}$. Note that t_0 is chosen such that $\tilde{\tau}_{\text{col}} = (\tilde{\rho}\tilde{v})^{-1}$. Although the gravitational potential Φ does not appear explicitly in the fluid equations, it is used in setting the adiabatic initial conditions. Therefore, we also define a corresponding, and consistent scaling quantity Φ_0 . The dimensionless gravothermal equations are

$$\partial_{\tilde{r}} (\tilde{\rho}_\chi \tilde{v}_\chi^2) = -\frac{\tilde{M}_{\text{pot}} \tilde{\rho}_\chi}{\tilde{r}^2} \quad (\text{S12})$$

$$\tilde{L} = -\frac{3}{2} \tilde{r}^2 \tilde{v}_\chi \left(\frac{1}{C_{\text{lmfp}}} \frac{1}{\tilde{r}^2 \tilde{\rho}_\chi^2} + \frac{\tilde{\sigma}_m^2}{C_{\text{smfp}}} \right)^{-1} \partial_{\tilde{r}} \tilde{v}_\chi^2 \quad (\text{S13})$$

$$\partial_{\tilde{r}} \tilde{L} = -\tilde{r}^2 \tilde{\rho}_\chi \tilde{v}_\chi^2 \partial_{\tilde{t}} \left(\ln \frac{\tilde{v}_\chi^3}{\tilde{\rho}_\chi} \right) \quad (\text{S14})$$

Therefore the transition between LMFP and SMFP happens when

$$\tilde{\rho}_\chi \simeq \sqrt{\frac{C_{\text{smfp}}}{C_{\text{lmfp}}}} \frac{1}{\tilde{r}\tilde{\sigma}_m} \quad (\text{S15})$$

Gaussian Potential Well and Adiabatic Initial Condition

We model the gravitational potential well with a Gaussian density profile: $\rho_{\text{pot}} = \rho_\star \exp(-r^2/2R_\star^2)$, which implies a total mass of $M_\star = (2\pi R_\star^2)^{3/2} \rho_\star$. The dimensionless quantities used in our numerical computation are

$$\tilde{M}_{\text{pot}}(\tilde{r}) = \tilde{M}_\star \left[\text{erf}\left(\frac{\tilde{r}}{\sqrt{2}\tilde{R}_\star}\right) - \sqrt{\frac{2}{\pi}} \frac{\tilde{r}}{\tilde{R}_\star} \exp\left(-\tilde{r}^2/2\tilde{R}_\star^2\right) \right] \quad (\text{S16})$$

$$\frac{d\tilde{M}_{\text{pot}}(\tilde{r})}{d\tilde{r}} = \tilde{M}_\star \sqrt{\frac{2}{\pi}} \frac{\tilde{r}^2}{\tilde{R}_\star^3} \exp\left(-\tilde{r}^2/2\tilde{R}_\star^2\right) \quad (\text{S17})$$

$$\tilde{\Phi} = \tilde{M}_\star \left[-\frac{1}{\tilde{r}} \text{erf}\left(\frac{\tilde{r}}{\sqrt{2}\tilde{R}_\star}\right) \right] \quad (\text{S18})$$

For the adiabatic initial condition, we use

$$\tilde{T}_m(\tilde{r}) = \tilde{T}_m^\infty - \frac{2}{5} \tilde{\Phi}(\tilde{r}) e^{-\tilde{r}^2/\tilde{\lambda}_{\text{grav}}^2} \quad (\text{S19})$$

$$\tilde{\rho}(\tilde{r}) = \tilde{\rho}_\chi^\infty \frac{1}{\tilde{T}_m(\tilde{r})} e^{-\int_\infty^{\tilde{r}} d\tilde{r}' \frac{\partial_{\tilde{r}'} \tilde{\Phi}(\tilde{r}')}{\tilde{T}_m(\tilde{r}')}} \quad (\text{S20})$$

Choices for Scaling Quantities and Mapping Simulation Input Parameters to Physical Parameters

We make the following choices, which determine the physical interpretation of the input dimensionless parameters:

$$M_0 = M_\star \quad (\text{S21})$$

$$\rho_0 = \rho_{\text{CDM}} \quad (\text{S22})$$

$$r_0 = \frac{GM_0}{v_\infty^2} \quad (\text{S23})$$

Given these three choices, we compute the rest of the scaling quantities

$$v_0 = \sqrt{GM_0/r_0} = v_\infty \quad (\text{S24})$$

$$t_0 = 6.6 \times 10^{-11} \text{ Gyr} \left(\frac{10^{10} \text{ cm}^2/\text{g}}{\sigma_m} \right) \left(\frac{0.4 \text{ GeV}/\text{cm}^3}{\rho_{\text{CDM}}} \right) \left(\frac{10^{-3}}{v_\infty} \right) \quad (\text{S25})$$

$$\sigma_0 = 9.5 \times 10^{12} \text{ cm}^2/\text{g} \left(\frac{0.4 \text{ GeV}/\text{cm}^3}{\rho_{\text{CDM}}} \right) \left(\frac{M_\odot}{M_\star} \right) \left(\frac{v_\infty}{10^{-3}} \right)^2 \quad (\text{S26})$$

Given these scaling quantities, we can compute dimensionless parameters

$$\tilde{M}_\star = M_\star/M_0 = 1 \quad (\text{S27})$$

$$\tilde{\lambda}_{\text{grav}} = (GM_\star/T_m^\infty)/r_0 = 1 \quad (\text{S28})$$

$$\tilde{\rho}_\chi^\infty = \rho_\chi^\infty/\rho_{\text{CDM}} = f_\chi \quad (\text{S29})$$

$$\tilde{R}_\star = R_\star/r_0 = 2v_0^2/v_{\text{esc}}^2 = 2\tilde{v}_{\text{esc}}^{-2} \quad (\text{S30})$$

TABLE I. Benchmark properties of compact objects.

	$M_{\text{ext}} [M_{\odot}]$	$R_{\text{ext}} [\text{km}]$	$r_0 [R_{\odot}]$	v_{esc}	\tilde{M}_{ext}	\tilde{R}_{ext}	\tilde{v}_{esc}
white dwarf	1	6000	2.12	0.02	1	4.0×10^{-3}	20
neutron star	1.4	10	2.97	0.6	1	4.8×10^{-6}	600

Modifications to the Original Codebase of [S50]

We adapt the original code base with the following modifications to make it suitable for the scenarios studied in this work:

- The original code base models self-gravitating systems; we modify it to use a fixed gravitational potential that is independent of the dark matter distribution. In other words, we neglect the gravitational influence of the dark matter relative to that of the central compact object.
- We update the gravitational scale height, and consequently the effective conductivity. In the original code base, the scale height is defined as $H = \sqrt{T/4\pi G\rho}$, which follows from the assumption of a self-gravitating system. In our case, as justified above, we instead set $H = r$.
- As explained in Appendix A of [S47], hydrostatic equilibrium is achieved through a linearized hydrostatic condition, expressed in the form of a tridiagonal equation $a_i d\tilde{r}_{i-1} + b_i d\tilde{r}_i + c_i d\tilde{r}_{i+1} = d_i$. We need to modify the coefficients a_i , b_i , c_i , and d_i to account for the fact that the external gravitational potential (and its corresponding mass distribution) is fixed. As a consequence, the mass enclosed within the i th shell changes as the shells move, unlike the self-gravitating case where each shell is defined with a fixed mass and the enclosed mass remains constant throughout the simulation. To account for this effect, we apply the following modification proportional to $d\tilde{M}_*(\tilde{r})/d\tilde{r}$ in the linearized hydrostatic condition equation:

$$b_i = b_i \Big|_{\text{original codebase}} + \frac{d\tilde{M}_*(\tilde{r})}{d\tilde{r}} \Big|_{\tilde{r}=\tilde{r}_i} \frac{1}{\tilde{r}_i} (\tilde{r}_i^3 - \tilde{r}_{i-1}^3)(\tilde{r}_i^3 - \tilde{r}_{i+1}^3)(\tilde{\rho}_i + \tilde{\rho}_{i+1})(\tilde{r}_{i-1} - \tilde{r}_{i+1}) \quad (\text{S31})$$

Without this additional linear term, the hydrostatic adjustment step following each heat conduction iteration converges slowly—if at all—in the simulations.

- Eq. S13 is consistent with Eq. (A1d) of [S47] (taking into account the modified scale height in our work). However, in the original codebase [S50], the definition of κ_{eff} appears to be missing an overall factor of $a\sigma_m$ (independently of the choice of H) relative to the definition of the paper κ_{paper} : $\kappa_{\text{code}}/a\sigma_m = \kappa_{\text{paper}}$. We implement Eq. S13 in our code.

LATE-TIME EVOLUTION

A common feature in all our gravothermal simulations is the formation of an isothermal core within which the temperature gradient of χ is suppressed, $|\partial_r T_m| \ll T_m/r$. Heuristically, this is due to the temperature-smoothing tendency of heat conduction, which is most efficient near the central region. We approximate the isothermal core as a ball of radius r_{iso} with a uniform temperature T_m^{iso} . In general, this core is surrounded by an exterior cloud whose temperature profile is $T_m^{\text{ext}}(r)$. Thus, the full temperature and density profiles read

$$T_m(r) = T_m^{\text{iso}} \Theta(r_{\text{iso}} - r) + T_m^{\text{ext}}(r) \Theta(r - r_{\text{iso}}) \quad (\text{S32})$$

$$\rho_\chi(r) = \rho_\chi^{\text{iso}} \Theta(r_{\text{iso}} - r) + \rho_\chi^{\text{ext}}(r) \Theta(r - r_{\text{iso}}) \quad (\text{S33})$$

Once the full temperature profile $T_m(r)$ is set, all the other relevant quantities can be derived from it. For instance, the density profile is given by the hydrostatic equilibrium Eq. (1). We define r_{iso} to be the radius that satisfies

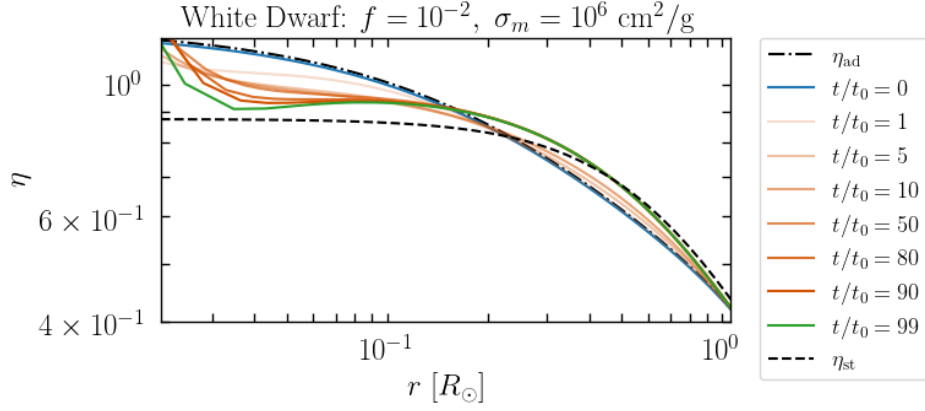


FIG. S1. Snapshots of simulated η profile (defined in Eq. S39) for a subcomponent pile around the benchmark white dwarf of Table I. The radius r from the center of the white dwarf ranges from r_{iso} (defined in Eq. S38) to λ_{grav} (defined in Eq. (S39)). The scale time t_0 is defined in Eq. (S25). Also shown are the adiabatic and steady profiles, $\eta_{\text{ad}}(r)$ and $\eta_{\text{st}}(r)$, defined in Eq. (S42) and (S43). It can be seen that the simulated η profile begins with $\eta_{\text{ad}}(r)$ and approaches $\eta_{\text{st}}(r)$.

$\partial_r T_m^{\text{ext}}|_{r=r_{\text{iso}}} = (T_m^\infty - T_m^{\text{iso}})/r_{\text{iso}}$. Integrating the gravothermal equations from $r = 0$ to $r = r_{\text{iso}}$ leads to the following heat equation for the isothermal core

$$\dot{T}_m^{\text{iso}} C_{\text{iso}} = -L_{\text{iso}} \quad (\text{S34})$$

The effective heat capacity of the isothermal core C_{iso} , the luminosity emerging from the isothermal core L_{iso} , the isothermal-core density $\rho_\chi^{\text{iso}}(r)$, and isothermal-core radius r_{iso} are given by

$$C_{\text{iso}} \equiv \int_0^{r_{\text{iso}}} 4\pi r^2 dr \rho_\chi^{\text{iso}} \left(\frac{3}{2} - \frac{\partial \ln \rho_\chi^{\text{iso}}}{\partial \ln T_m^{\text{iso}}} \right) = \int_0^{r_{\text{iso}}} 4\pi r^2 dr \rho_\chi^{\text{iso}} \left(2\eta_{\text{iso}} + \frac{1}{2} + \frac{-\Phi}{T_m^{\text{iso}}} \right) \quad (\text{S35})$$

$$L_{\text{iso}} \equiv 4\pi r_{\text{iso}}^2 [\kappa_{\text{eff}}^{\text{ext}} \partial_r T_m^{\text{ext}}]_{r=r_{\text{iso}}} = -\frac{6\pi C_{\text{lfp}} \sigma_m r_{\text{iso}}^3 [\rho_\chi(r_{\text{iso}})]^2 \sqrt{T_m^{\text{iso}}} (T_m^{\text{iso}} - T_m^\infty)}{1 + (C_{\text{lfp}}/C_{\text{smfp}})[\rho_\chi(r_{\text{iso}})\sigma_m r_{\text{iso}}]^2} \quad (\text{S36})$$

$$\rho_\chi^{\text{iso}}(r) = \left(\rho_\chi^\infty \frac{T_m^\infty}{T_m^{\text{iso}}} e^{-\int_\infty^{r_{\text{iso}}} \frac{dr'}{r'} \frac{GM_\star}{T_m(r')}} \right) e^{-\frac{\Phi(r) - \Phi(r_{\text{iso}})}{T_m^{\text{iso}}}} = \rho_\chi^\infty (2\eta_{\text{iso}})^{2\bar{\eta}} \left(\frac{T_m^{\text{iso}}}{T_m^\infty} \right)^{2\bar{\eta}-1} e^{-\frac{\Phi(r)}{T_m^{\text{iso}}} - 2\eta_{\text{iso}}} \quad (\text{S37})$$

$$r_{\text{iso}} = \frac{GM_\star}{2\eta_{\text{iso}} T_m^{\text{iso}}} \quad (\text{S38})$$

In writing the above, we defined

$$\eta \equiv \frac{GM_\star/r}{2T_m^{\text{ext}}}, \quad \eta_{\text{iso}} \equiv \eta(r_{\text{iso}}), \quad \bar{\eta} \equiv \frac{\int_{r_{\text{iso}}}^\infty \eta dr/r}{\int_{r_{\text{iso}}}^{\lambda_{\text{grav}}} dr/r}, \quad \lambda_{\text{grav}} \equiv \frac{GM_\star}{T_m^\infty} \quad (\text{S39})$$

where we have assumed $\Phi(r_{\text{iso}}) \approx -GM_\star/r_{\text{iso}}$. In solving Eq. (S34), we will choose the initial condition such that $T_m^{\text{iso}}(t=0) \approx T_m^{\text{ad}}(r=R_\star)$. Nevertheless, the late-time profiles are insensitive to the precise choice of initial condition.

The exterior profiles, T_m^{ext} and ρ_χ^{ext} , are in principle history-dependent and can only be found by evolving the initial adiabatic profiles with the gravothermal equations. However, our simulations show that the exterior profiles evolve in a rather simple way: they interpolate between two profiles, (1) the initial *adiabatic* profile and (2) a uniform-luminosity solution we call the *steady* profile. The associated temperature profiles can be approximated as

$$T_m^{\text{ad}}(r) = T_m^\infty + \frac{2GM_\star}{5r} e^{-\frac{r^2}{\lambda_{\text{grav}}^2}}, \quad (\text{adiabatic}) \quad (\text{S40})$$

$$T_m^{\text{st}}(r) = T_m^\infty + \frac{4GM_\star}{7r} e^{-\frac{7r}{4\lambda_{\text{grav}}}}, \quad (\text{steady}) \quad (\text{S41})$$

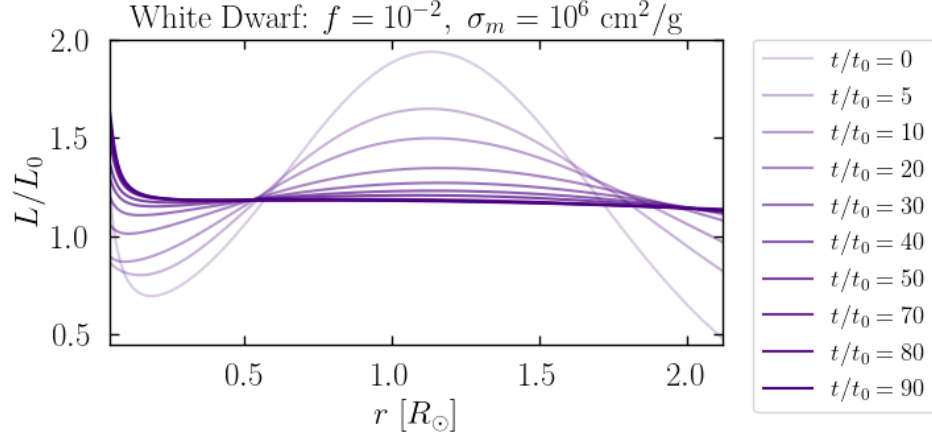


FIG. S2. Snapshots of simulated outward heat-conduction luminosity L profiles (defined in Eq. (S2)) for a subcomponent pile around the benchmark white dwarf of Table I. The radius r from the center of the white dwarf ranges from r_{iso} (defined in Eq. S38) to λ_{grav} (defined in Eq. (S39)). The scale quantities L_0 and t_0 are defined in Eqs. (S9), (S22)(S24), (S25), and (S26). It can be seen that the L profile evolves toward and settles at a spatially-uniform steady-state.

At $r \gg R_*$, these profiles correspond to

$$\eta_{\text{ad}}(r) = \frac{5/4}{e^{-\frac{r^2}{\lambda_{\text{grav}}^2}} + \frac{5r}{2\lambda_{\text{grav}}}}, \quad \eta_{\text{ad}}^{\text{iso}} \approx \frac{5/4}{e^{-\frac{4(T_m^{\text{iso}})^2}{25(T_m^{\text{iso}} - T_m^{\infty})^2}} + \frac{T_m^{\infty}}{T_m^{\text{iso}} - T_m^{\infty}}}, \quad \bar{\eta}_{\text{ad}} \approx \frac{5}{4} \left[1 + \frac{\ln(0.46 + \frac{r_{\text{iso}}}{\lambda_{\text{grav}}})}{\ln(\lambda_{\text{grav}}/r_{\text{iso}})} \right] \approx 0.9 - 1.1 \quad (\text{S42})$$

$$\eta_{\text{st}}(r) = \frac{7/8}{e^{-\frac{7r}{4\lambda_{\text{grav}}}} + \frac{7r}{4\lambda_{\text{grav}}}}, \quad \eta_{\text{st}}^{\text{iso}} \approx \frac{7/8}{e^{-\frac{T_m^{\infty}}{T_m^{\text{iso}} - T_m^{\infty}}} + \frac{T_m^{\infty}}{T_m^{\text{iso}} - T_m^{\infty}}}, \quad \bar{\eta}_{\text{st}} \approx \frac{7}{8} \left[1 + \frac{\ln(1.15 + \frac{r_{\text{iso}}}{\lambda_{\text{grav}}})}{\ln(\lambda_{\text{grav}}/r_{\text{iso}})} \right] \approx 0.9 \quad (\text{S43})$$

The expressions of η_{ad} and η_{iso} are exact for the temperature profiles in Eq. (S40)&(S41); $\eta_{\text{ad}}^{\text{iso}}$ and $\eta_{\text{st}}^{\text{iso}}$ are valid in the limit $r_{\text{iso}} \ll \lambda_{\text{grav}}$; $\bar{\eta}_{\text{ad}}$ and $\bar{\eta}_{\text{st}}$ do not have closed-form expressions, so we instead show functions that provide good fits to their numerical values. We note that all these η 's are close to unity, especially when $T_m^{\text{iso}}/T_m^{\infty}$ is not exceedingly large. This justifies the simplifying assumption we made in the main text, where we took $\eta_{\text{iso}} = \bar{\eta} = \eta_{\text{eff}} = 1$. We display in Fig. S2 how the simulated η profile evolves from $\eta_{\text{ad}}(r)$ toward $\eta_{\text{st}}(r)$.

Let us now describe the origin of the steady profile $T_m^{\text{st}}(r)$ in Eq. (S41), which is valid when the external profiles are in the long mean free path (LMFP) regime, $\lambda_{\text{mfp}} \gg r$. As can be seen in Fig. S1, the simulated luminosity L evolves from the initial profile toward uniformity. The temperature profile in Eq. (S41) corresponds to this eventual uniform-luminosity steady state. Eliminating ρ_χ from the hydrostatic equilibrium Eq. (1) and assuming the LMFP luminosity is uniform $L \propto r^4 \rho_\chi^2 \sqrt{T_m^{\text{ext}}} \partial_r T_m^{\text{ext}} = \text{uniform}$, we find the following differential equation for the external temperature profile T_m^{ext}

$$\frac{\partial_r^2 T_m^{\text{ext}}}{\partial_r T_m^{\text{ext}}} - \frac{3\partial_r T_m^{\text{ext}}}{2T_m^{\text{ext}}} + \frac{4}{r} \left(1 - \frac{GM_*/r}{2T_m^{\text{ext}}} \right) = 0 \quad (\text{S44})$$

The solutions to this nonlinear differential equation can be found numerically with techniques such as the shooting method, and are well fitted by Eq. (S41). A special case of this solution can be derived with the following simple scaling argument. At radii r intermediate between r_{iso} and λ_{grav} , we expect the solution to be scale-free. Substituting a power-law ansatz to the above equation $T_m^{\text{ext}} = Cr^{-n}$, we find that $T_m^{\text{st}} \approx 4GM_*/7r$ (which implies $\rho_\chi^{\text{ext}} \propto r^{-3/4}$) is the only solution. Eq. (S41) is a generalization of this scale-free solution that captures the behavior at $r \sim r_{\text{iso}}$ and $r \sim \lambda_{\text{grav}}$ more accurately.

The tendency of the temperature profile to approach T_m^{ext} can be understood partially as follows. Initially, at $t \ll \tau_{\text{cond}}(r_{\text{iso}})$, heat transfer in the exterior cloud is still inefficient, and so the exterior profiles remain adiabatic, $T_m^{\text{ext}}(r) = T_m^{\text{ad}}(r)$ and $\rho_\chi^{\text{ext}}(r) = \rho_\chi^{\text{ad}}(r)$. Then the gravothermal equations dictate that the direction of evolution is such that the magnitude of the luminosity gradient $|\partial_r L|$ decreases over time. As this happens, the rate at which the specific entropy increases, $\dot{s} \propto -\partial_r L$, becomes slower. Eventually the evolution of s and hence the entire exterior

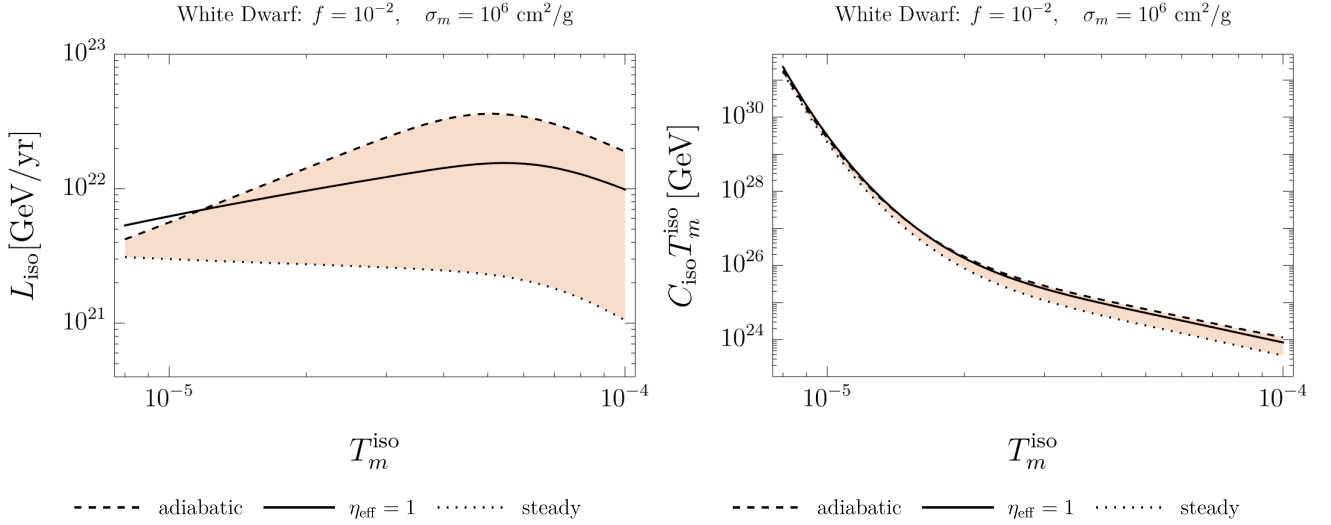


FIG. S3. Thermal properties of the isothermal core of a pile of subcomponent with $(f, \sigma_m) = (10^{-2}, 10^6 \text{ cm}^2/\text{g})$ around the benchmark white dwarf of Table I. *Left*: Outward heat conduction luminosity emerging from the isothermal core L_{iso} (defined in Eq. (S36)) as a function of the isothermal-core temperature T_m^{iso} . *Right*: The product between the isothermal core's heat capacity (defined in Eq. (S35)) and temperature $C_{\text{iso}} T_m^{\text{iso}}$ as a function of T_m^{iso} . The dashed, dotted, and solid lines represent three assumptions of $\eta \equiv r \partial_r \Phi / 2 T_m^{\text{ext}}$, namely the adiabatic and steady external profiles as defined in Eqs. (S40)&(S41) and $\eta_{\text{iso}} = \bar{\eta} = \eta_{\text{eff}} = 1$ assumed in the main text, with $\eta_{\text{iso}} = \bar{\eta}$ defined in Eq. (S39).

profile essentially freezes when $|\partial_r L|$ is small, i.e., when L is approximately uniform. In short, the uniform-luminosity solution appears to be an attractor because the system initially approaches it and slows down when close to it. Uniform-luminosity solutions are also found both analytically and numerically, as dynamical attractors, in other astrophysical systems with similar physics, including the interior of various stars. The $\rho_\chi \propto r^{-3/4}$ can be thought of as a velocity-independent σ_m analog of the well-known Bahcall-Wolf solution [S51], which applies for a gas with a Coulombic velocity-dependent cross-section $\sigma_m \propto v^{-4}$.

In general, the external temperature profile $T_m^{\text{ext}}(r)$ is somewhere between adiabatic profile $T_m^{\text{ad}}(r)$ and the steady profile T_m^{st} . We plot the corresponding heat capacity C_{iso} of the isothermal core and the luminosity emerging from it L_{iso} in Fig. S3. For the most part, the L_{iso} is larger for the adiabatic profile than for the steady profile, while their C_{iso} are nearly the same. These amount to the temperature evolution rate $\dot{T}_m^{\text{iso}}/T_m^{\text{iso}} = -L_{\text{iso}}/(C_{\text{iso}} T_m^{\text{iso}})$ being faster in the adiabatic case. To show the range of possible evolutions, we numerically integrate the simplified heat equation, Eq. (S34), assuming these exterior solutions as two extreme cases. The resulting time-evolution of the central density $\rho_\chi(R_\star)$ is displayed in Fig. S4. In addition, we include in the same figure the central density evolution corresponding to the simplification $\eta_{\text{iso}} = \bar{\eta} = \eta_{\text{eff}} = 1$ used in the main text. All the solutions imply that as T_m^{iso} cools down, the central density profile $\rho_\chi(R_\star)$ rises approximately linearly in time, increasing the heat capacity of the isothermal core C_{iso} exponentially, and making it progressively harder to cool T_m^{iso} further.

PARTICLE PHYSICS MODELS

Here, we present concrete particle physics models as existence proofs and discuss their relevant model-dependent phenomenology.

Dark Scalar

The subcomponent χ considered in the main text could be a scalar χ with the following Lagrangian

$$\mathcal{L}_\chi = \frac{1}{2} (\partial\chi)^2 - \frac{1}{2} m_\chi^2 \chi^2 - \frac{\lambda_\chi}{4} \chi^4 \quad (\text{S45})$$

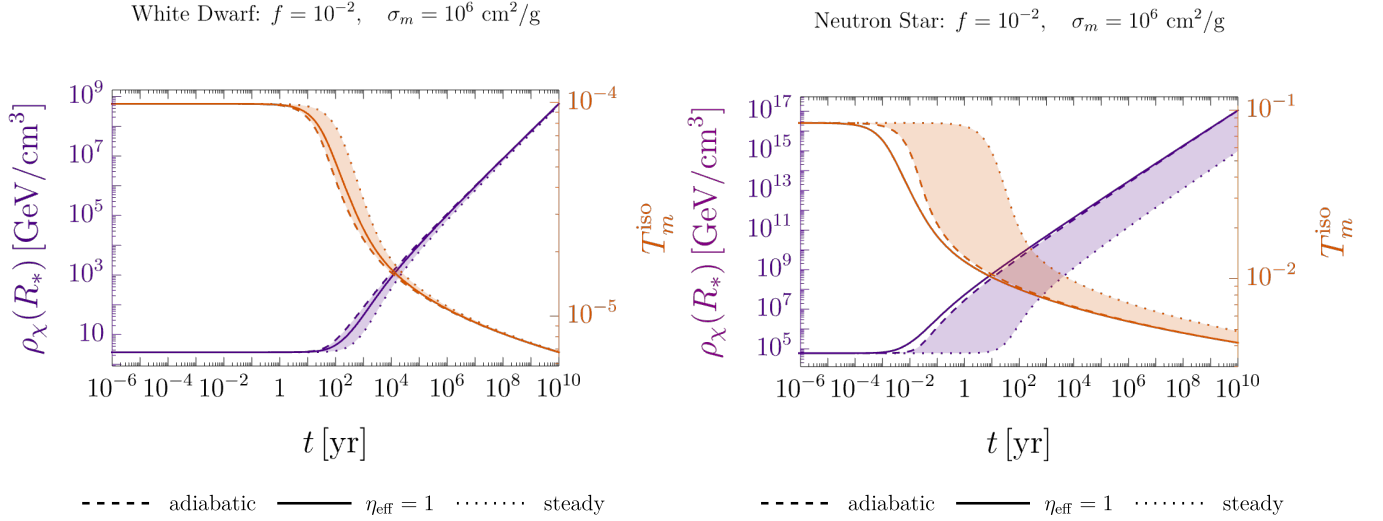


FIG. S4. Time-evolution of the density $\rho_\chi(R_*)$ of piles of subcomponent with $(f, \sigma_m) = (10^{-2}, 10^6 \text{ cm}^2/\text{g})$ around the benchmark WD (*left*) and NS (*right*) of Table I evaluated at the respective compact-object radii R_* . The results are obtained by integrating Eq. (S34) using the isothermal-core properties given in Eqs. (S35), (S36), (S37), (6), (S42), and (S43). The dashed, dotted, and solid lines represent three assumptions of $\eta \equiv r\partial_r\Phi/2T_m^{\text{ext}}$, namely the adiabatic and steady external profiles as defined in Eqs. (S40)&(S41) and $\eta_{\text{iso}} = \bar{\eta} = \eta_{\text{eff}} = 1$ assumed in the main text, with η_{iso} and $\bar{\eta}$ defined in Eq. (S39).

The non-relativistic self-scattering cross section per unit mass in this model is

$$\sigma_m = \frac{9\lambda_\chi^2}{32\pi m_\chi^3} = 2 \times 10^4 \lambda_\chi^2 \text{ cm}^2/\text{g} \left(\frac{m_\chi}{\text{MeV}} \right)^{-3} \quad (\text{S46})$$

To ensure vacuum stability and perturbativity, the self coupling must lie in the range $0 < \lambda_\chi < 16\pi$, which implies that in order for the scalar to have a large σ_m it needs to be sufficiently light. Light particles tend to have large de-Broglie wavelengths and are thus prone to overlap. The phase-space density \mathcal{F} of χ at galactic scales is

$$\mathcal{F}_{\text{gal}} = \frac{\rho_\chi^\infty/m_\chi}{(m_\chi\sqrt{T_m})^3} \sim 0.2f \left(\frac{T_m}{10^{-6}} \right)^{-3/2} \left(\frac{m_\chi}{10 \text{ eV}} \right)^{-4} \quad (\text{S47})$$

During the gravothermal evolution, \mathcal{F} may increase by orders of magnitude. While number-changing processes such as $\chi\chi\chi\chi \rightarrow \chi\chi$ may prevent it from reaching unity, such processes could also be turned off by making the scalar a complex field and populating it asymmetrically, with only particles and no antiparticles [S123, S124]. The scalar χ could also be composite. It could represent, e.g., dark glueballs of a confined Yang-Mills sector [S60, S61, S70] whose cubic self-interaction ϕ^3 allows for $\chi\chi\chi \rightarrow \chi\chi$ number-changing processes. We show the parameter space of the dark scalar model in Fig. S5.

If the χ particles are produced relativistically, they can subsequently self-thermalize through $2 \rightarrow 4$ number-changing processes of the form $\chi\chi \rightarrow \chi\chi\chi\chi$ [S58]. Assuming the χ sector is in a kinetic equilibrium with a temperature T' , the cross-section for this process when χ is non-relativistic and relativistic are $\langle\sigma_{2\rightarrow 4}v\rangle \sim \lambda_\chi^4/m_\chi^2$ and $\langle\sigma_{2\rightarrow 4}v\rangle \propto T'^{-2}$, respectively, where T' is the dark sector temperature. This implies that the thermalization efficiency $n_\chi \langle\sigma_{2\rightarrow 4}v\rangle H^{-1}$ is maximized at $T' \sim m_\chi$. Requiring $n_\chi \langle\sigma_{2\rightarrow 4}v\rangle H^{-1}|_{T'=m_\chi} \gtrsim 1$, we find that the χ sector would self-thermalize if

$$\lambda_\chi \gtrsim \xi_s^{-1/6} \left(\frac{m_\chi}{M_{\text{Pl}}} \right)^{1/4} = 5 \times 10^{-6} \xi_s^{-1/6} \left(\frac{m_\chi}{\text{MeV}} \right)^{1/4} \quad (\text{S48})$$

where $M_{\text{Pl}} = 2 \times 10^{18} \text{ GeV}$ is the reduced Planck mass and $\xi_s \equiv s'/s$ is the ratio between the entropy densities of χ and the SM after the χ sector is self-thermalized. This is a conserved quantity as long as the χ sector remains self-thermalized and decoupled from the SM sector. Since we are mainly interested in χ with a large self coupling, we will assume that the above self-thermalization condition is satisfied. Once thermalized, the χ sector will remain thermalized until the rate of $4 \rightarrow 2$ processes $n_\chi^3 \langle\sigma_{4\rightarrow 2}v^3\rangle$ drops below Hubble, whereupon n_χ freezes out, typically

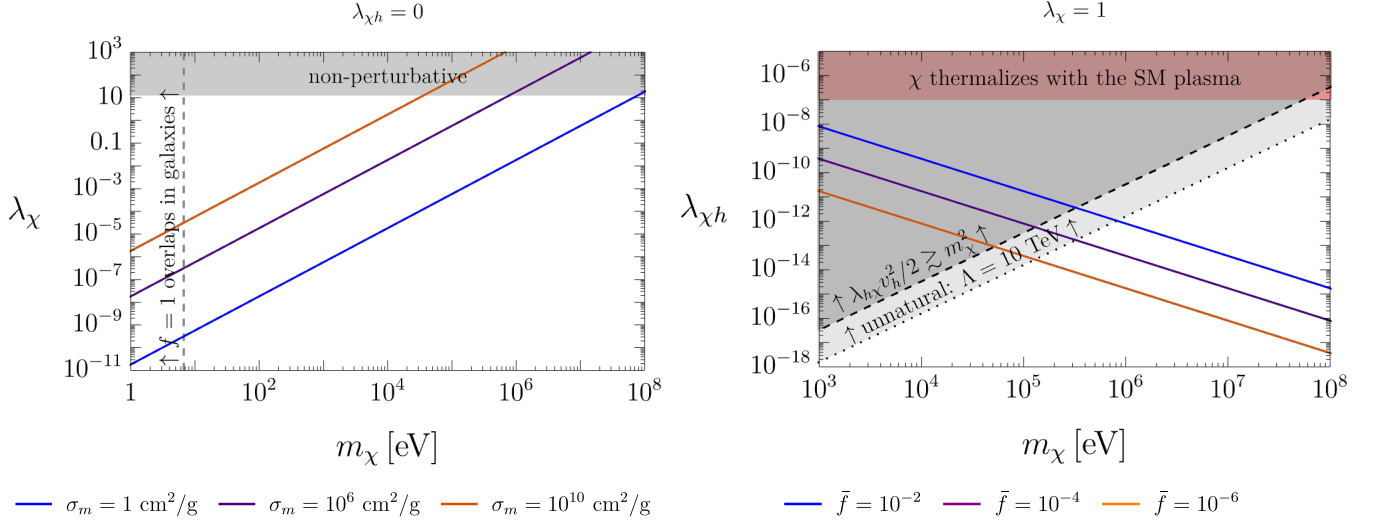


FIG. S5. Dark scalar parameter space. *Left*: Self-coupling λ_χ vs mass m_χ space in the absence of a higgs-portal, $\lambda_{\chi h} = 0$. In the gray region, the λ_χ is non-perturbative. To the left of the dashed line the galactic population of $f = 1$ scalars have occupation number greater than unity. Colored lines correspond to different values of σ_m . *Right*: Higgs-portal coupling $\lambda_{\chi h}$ vs mass m_χ for self-coupling $\lambda_\chi = 1$. In the red region, χ particles achieve full thermalization with the SM plasma in the early universe. In the gray regions, a tuning of parameters is needed to keep m_χ light. Color lines correspond to different cosmic DM fractions \bar{f} of χ today.

at $T' \sim m_\chi/10$. The resulting cosmic relic DM fraction of χ today is [S55]

$$\bar{f} \approx 2 \times 10^5 \xi_s \left(\frac{m_\chi}{\text{MeV}} \right) \quad (\text{S49})$$

The value of ξ_s depends on the way in which the χ sector is populated. Even if the χ particles are decoupled from the SM, an abundance of χ could also arise, for instance, through asymmetric reheating [S125, S126]. They could also be produced through a gravitational production mechanism during or at the end of inflation [S127–S129]. While some of these scenarios are subject to isocurvature-perturbation constraints from CMB observations, they are much less severe for a subcomponent.

Next, we mention several consequences of coupling χ with the SM. As an example, we consider the following Higgs-portal coupling

$$V_{\chi h} = \frac{\lambda_{\chi h}}{2} \chi^2 \mathcal{H}^\dagger \mathcal{H} \quad (\text{S50})$$

where \mathcal{H} is the Standard Model Higgs doublet, and we have removed the cubic Higgs-portal coupling $A\chi\mathcal{H}^\dagger\mathcal{H}$ by imposing a \mathbb{Z}_2 symmetry, under which $\chi \rightarrow -\chi$. This implies that indirect-detection signals will be dominated by annihilation instead of decay. A consequence of introducing the above coupling is that the χ particles will receive mass-squared contributions through it. At tree level, we have $m_\chi^2 = \mu_\chi^2 + \lambda_{\chi h} v_h^2/2$ with $v_h = 246 \text{ GeV}$. We assume that $m_\chi^2 > 0$ in order to keep $\langle \chi \rangle = 0$, ensuring the stability of the χ particles. Furthermore, quantum corrections are expected to contribute $\delta m_\chi^2 \gtrsim \lambda_{\chi h} \Lambda^2/16\pi^2$ to χ 's mass squared. To avoid fine-tuning, we require $m_\chi^2 > \max(\lambda_{\chi h} v_h^2/2, \lambda_{\chi h} \Lambda^2/16\pi^2)$. A large σ_m requires a small m_χ since λ_χ is limited by perturbativity. A small m_χ , in turn, requires a correspondingly small $\lambda_{\chi h}$ in order to keep m_χ small. See Fig. S5.

The dominant production channel of χ in the early universe is through higgs boson decay $h \rightarrow \chi\chi$, whose rate is $\Gamma_{h \rightarrow \chi\chi} = \lambda_{\chi h}^2 v_h^2/32\pi m_h$, where the higgs mass is $m_h = 125 \text{ GeV}$. These decays occur mostly at $T \sim m_h/3$. If $\Gamma_{h \rightarrow \chi\chi} H^{-1} \gtrsim 1$ at that time, which amounts to $\lambda_{\chi h} \gtrsim 10^{-7}$, then χ reaches a thermal equilibrium with the SM plasma. The later case is ruled out by the combination of collider and direct detection constraints [S130, S131], so we focus on the freeze-in scenario with $\lambda_{\chi h} \lesssim 10^{-7}$ here. The initial freeze-in energy density of χ can be estimated as $\rho_{h \rightarrow \chi\chi} \sim [m_h(m_h T)^{3/2} e^{-m_h/T} \Gamma_{h \rightarrow \chi\chi} H^{-1}]_{T=m_h/3}$. This leads to the following entropy ratio after self-thermalization

of χ

$$\xi_s = \frac{s'}{s} \sim \left(\frac{\rho_{h \rightarrow \chi\chi}}{\rho_{\text{crit}}} \right)_{T=m_h/3}^{3/4} \sim 5 \times 10^{-6} \left(\frac{\lambda_{\chi h}}{10^{-10}} \right)^{3/2} \quad (\text{S51})$$

From this and Eq. (S49), we estimate the present-epoch cosmic DM fraction of χ to be

$$\bar{f} \sim \left(\frac{\lambda_{\chi h}}{10^{-10}} \right)^{3/2} \left(\frac{m_\chi}{\text{MeV}} \right) \quad (\text{S52})$$

Dark Atom

Consider a QED-like theory with the following Lagrangian

$$\mathcal{L}_{\text{dQED}} = -\frac{1}{4} F'_{\mu\nu} F'^{\mu\nu} + \bar{p}' (i\not{\partial} + g' \not{A} + m_{p'}) p' + \bar{e}' (i\not{\partial} - g' \not{A} - m_{e'}) e' \quad (\text{S53})$$

This theory includes a hidden $U(1)'$ gauge field A'_μ whose field strength tensor is $F'_{\mu\nu}$, a dark proton p' of mass $m_{p'}$ and $U(1)'$ charge $+g'$, and a dark electron e' of mass $m_{e'}$ and $U(1)'$ charge $-g'$, [S64, S65, S69]. A dark proton and a dark electron can bind to form a hydrogen-like dark atom H' with Bohr radius $a'_0 = (\alpha' \mu_{H'})^{-1}$ and binding energy $B' = \alpha'^2 \mu_{H'}/2$, where $\mu_{H'} = m_{e'} m_{p'} / (m_{e'} + m_{p'})$ is the p' - e' reduced mass and $\alpha' = g'^2/4\pi$ is the dark analogue of the fine-structure constant. If the binding energy B' is considerably larger than the highest temperature of the gravothermal analysis and the ionized fraction is tiny, dark atoms H' can play the role of the subcomponent with elastic self-interactions χ . Two dark atoms collide elastically with

$$\sigma_m \sim \frac{100 a_0^2}{m'_p} = 2 \times 10^6 \alpha'^2 \text{cm}^2/\text{g} \left(\frac{m_{p'}}{\text{GeV}} \right)^{-1} \left(\frac{m_{e'}}{100 \text{keV}} \right)^{-2} \quad (\text{S54})$$

for low momentum transfers and $m_{p'} \gg m_{e'}$. Notably, the composite nature of H' allows it to have a large σ_m with a relatively heavy $m_\chi = m_{H'} \approx m_{p'}$ compared to, e.g., the dark scalar model of the previous subsection. Alternatively, if the dominant DM is in the form of dark atoms, unpaired dark protons and dark electrons could play the role of subcomponents with large cross-sections, since dark-charged particles can have cross sections significantly larger than that of neutral dark atoms. The simplest way to populate the dark QED sector is, again, through asymmetric reheating or a gravitational production mechanism. CMB observations are sensitive to a dark QED sector that comprises a fraction as small as 5% of the total dark matter, if it is highly ionized and undergoes dark acoustic oscillations. However, if the dark QED sector is sufficiently cold and have negligible ionization fraction, such limits are considerably weakened. In that case, the subdominant dark electrons and dark protons would have velocity-dependent cross sections. Finally, to get non-gravitational signals, one could turn on kinetic mixing $\epsilon F^{\mu\nu} F'_{\mu\nu}/2$.